Adv Biochem Engin/Biotechnol (2005) 95: 201–243
DOI 10.1007/b102215

Deconvolution Microscopy

Jean-Baptiste Sibarita (✉)

Curie Institute, Research Division, UMR144-CNRS, 75005 Paris, France
sibarita@curie.fr

Abstract Since its introduction in 1983, deconvolution microscopy has become a key image-processing tool for visualizing the cellular structures of fixed and living specimens in three dimensions and at subresolution scale. The last 20 years have seen the development of many different applications based on deconvolution microscopy, including a wide variety of optical setup and deconvolution algorithms. This chapter aims to summarize and to describe

in detail the major features of this technology, from theoretical aspects to practical solutions. It will begin by explaining the principle of image formation in three-dimensional optical sectioning microscopy. As deconvolution microscopy provides, in essence, a means of overcoming the limits of optical microscopy, the second part of this chapter is dedicated to the theoretical and experimental description of image generation through a microscope. Methods will be detailed for the determination of point spread function, as a crucial step for the characterization of any optical system and a key preliminary step for image deconvolution. The challenges faced and the various possibilities for determining this function precisely will be discussed. All possible sources of aberrations and image degradation processes will be discussed. In the third part of this chapter, we will introduce the acquisition setup and requirements for compliance between acquisition and deconvolution processes. Typical setups for fixed and living cell observation will be detailed, with key features for optimizing speed and reducing artifacts. In the fourth and last part of this chapter, we will describe, in theoretical terms, the various restoration algorithms commonly used in the field of optical microscopy and will provide results obtained with some of the commercially available packages. We shall conclude by considering the prospects for future solutions (currently under development) aiming to handle more easily the huge amounts of data generated by rapid multi-dimensional living cell microscopy. Designed for use by standard cell biologists and hardware and software engineers and developers, this chapter has been written to provide a clear explanation of the wide-reaching and powerful domain of deconvolution microscopy.

Keywords Deconvolution · Wide-field microscopy · Confocal microscopy · Image restoration algorithm · Point spread function

1 Introduction

Light microscopy provides cell biologists with the unique possibility of examining living samples under conditions similar to those found in the native state. Recent progress in cellular, molecular biology and microscopy has made possible the acquisition of multidimensional data concerning rapid cellular activities. It is now feasible to observe the cellular activities of various organelles within the cell, in three dimensions, at high spatial and temporal resolutions. These observations are achieved by means of optical sectioning microscopy, in which images are recorded while the focal plane is rapidly and precisely raised through the sample. The three-dimensional (3D) acquisition process is repeated at several time points during a given period, leading to the collection of image stacks. This results in four-dimensional (4D) acquisition: three spatial dimensions plus the time dimension. The acquisition of multiple labels by means of such a technique is called five-dimensional microscopy (5D), with wavelength (λ) acting is the fifth dimension.

Living cell microscopy has undergone taken a major leap forward in the last ten years, thanks to the introduction of natural fluorescent probes such as green fluorescent protein (GFP) [2–4] and its derivatives (cyan FP, yellow FP, etc.). These advances, combined with increases in the sensitivity of high-resolution detectors, have made it possible to observe living cells for a long

period of time at low light excitation levels, minimizing the disturbance of cell activity.

The greatest limitation of optical microscopy is spatial resolution, which is in the range of the wavelength of light used. The ultimate goal of cell microscopy is to capture the activity of cell components. In this respect, the resolution of limited numerical aperture wide-field microscopy may not be sufficiently high to optically resolve small organelles. This results in blurring, each focal plane being contaminated with out-of-focus information from the adjacent planes above and below that examined, making the data difficult, if not impossible to analyze. Confocal scanning light microscopy (CSLM) [5, 6] and confocal spinning disk microscopy [7] both provide higher spatial resolution than conventional wide-field microscopy. Unfortunately, these techniques are slower and require higher levels of light excitation than wide-field microscopy. They are therefore not always compatible with the high-speed multi-dimensional living cell microscopy required for the observation of subcellular phenomena. Deconvolution is a computational restoration method that provides an alternative means of producing high-resolution images. Unlike confocal techniques, which physically remove the out-of-focus emission information by means of a pinhole, deconvolution is a mathematical processing method in which computations for the acquired stacks reassign the diffracted light to its original location. As the emitted signal is collected in its entirety by means of a highly sensitive CCD camera, post-deconvolution images may in some cases provide higher resolution than confocal microscopy. Moreover, the sensitivity and dynamic range of wide-field deconvolution microscopy are much higher than those of confocal microscopy, and this may prove critical for the observation of small, dark objects (e.g. vesicles or tubules) in the vicinity of larger, brighter structures (e.g. the Golgi apparatus).

Deconvolution is a heavy computational method now accessible to any laboratory, thanks to the fantastic progress of computer science. A stack of images can now be processed by inexpensive computers, in a time period as short as a few milliseconds to a few hours, depending on acquisition size and the deconvolution algorithm used. Moreover, spatial deconvolution is not strictly limited to wide-field microscopy. Instead, it can also be applied to confocal data, increasing resolution and facilitating more profound structural analysis.

The choice between the various techniques available depends on many parameters, including spatial and temporal resolution, spectral requirements, space and time observation windows, bleaching, and the available equipment. Regardless of the technique chosen, data collection must be optimized and an appropriate deconvolution algorithm selected [8, 9]. The deconvolution process is directly linked to the image formation process. The quality of deconvolution thus depends on the quality of the microscopy. This chapter aims to guide users through the fantastic and wide-ranging world of deconvolution microscopy.

2
Image Formation and Optical Distortions in Three-Dimensional Fluorescence Microscopy

Recent advances in fluorescence microscopy, detectors, motorization and digital image processing have made possible the routine collection of two- and three-dimensional data for biological samples. In three dimensions, the object is optically sectioned plane by plane in a process involving the continuous displacement of the focal plane along the optical axis (Fig. 1). The objective or the sample may be moved to change the focal plane and acquire the corresponding 2D section image. For living cell experiments, particularly if high speed sectioning is required, it is recommended to move the objective rather than the whole sample to prevent morphological changes in the object due to its displacement. Both confocal microscopy and wide-field microscopy involve optical sectioning. Confocal microscopy is based on the illumination of a small, highly focused and diffraction-limited volume with a beam of light, and detection of the fluorescence emitted from the excited volume with a single-element detector. A pinhole is placed in the plane of the image, just in front of the detector, to eliminate a portion of the out-of-focus light emitted, thereby increasing axial resolution. For each focal position, a two-dimensional image is captured point by point, by scanning this single spot in the observation plane. Although fundamentally different, both scanning confocal microscopy and wide-field microscopy are based on the same process of image formation produced by a point source object (Fig. 1).

Even the most perfect of objectives produces a distorted image of the object. The degradation observed during image formation is mostly due to optical blur and photon noise. Optical blur is a consequence of light diffraction through an optical system, resulting in the limitation of optical resolution. This limitation is physical and reproducible and is inherent to any optical system. It can be characterized both theoretically and experimentally, and a precise understanding of this limitation forms the basis of most deconvolution algorithms.

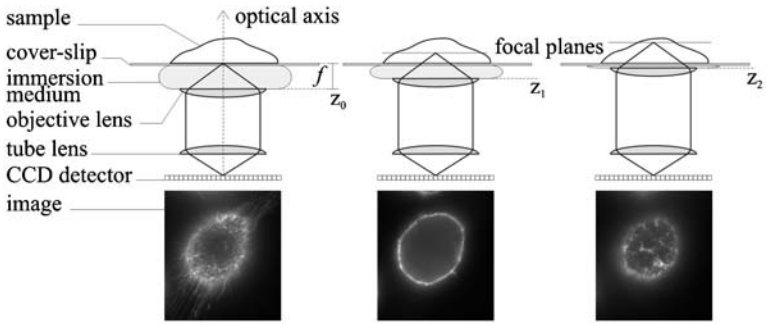

Fig. 1 Optical sectioning microscopy is performed by moving the focal plane of the objective along the optical axis. With infinite optics, the focal plane remains constant and located at a distance *f* from the objective, where *f* is the focal length of the objective

Noise is a random process that is also responsible for image degradation. In digital microscopy, noise arises from the statistical distribution of the photons and electronic devices. Both sources are known and have been described statistically [10]. Photons are the predominant source of noise. The quantum nature of light results in the detected photons following a Poisson distribution. The electronic noise is Gaussian in nature and is negligible in modern detectors in comparison to photon noise. This often results in image quality being purely a function of the number of detected photons, which depends on integration time and the quantum efficiency of the detector. The noise present in the image considerably limits the efficiency of deconvolution algorithms. It must be taken into account, either directly in the algorithms themselves, or by adapted filtering. The level of noise depends on the observation conditions. Most living cell acquisitions aiming to capture rapid 3D events have low signal-to-noise ratios, because cell viability and fluorescence must be preserved.

Figure 2 shows a simulation of an object subject to blur and noise degradation, as observed through a microscope. One very noticeable effect of the blur is the difference in intensity distribution between small and large objects.

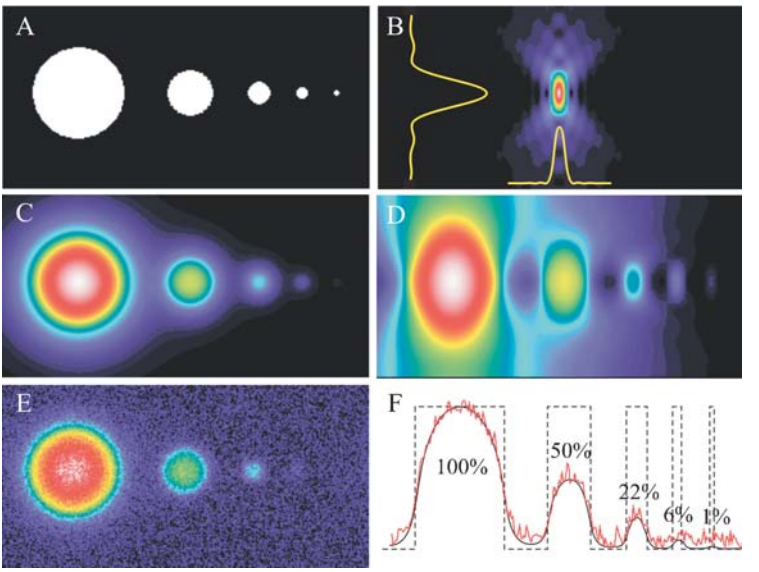

Fig. 2 Three-dimensional simulation of an object observed through a microscope, in the presence of optical blur and noise. The object consists of five spheres with different diameters but the same fluorescence density: **A** initial object; **B** point spread function (PSF) of the microscope; **C**, **D** lateral and axial cross sections of the object after convolution with the microscope's PSF; **E** lateral cross section of the object after blurring and the addition of noise; **F** intensity profiles and percentage of the object's maximum intensity of original (*dashed*), blurred (*black*) and blurred+noisy (*red*) data. Following blurring, the smaller the object, the weaker its maximum intensity is likely to be. Noise reduces the likelihood of detecting small and highly attenuated objects

2.1 Image Formation in an Ideal, Aberration-Free Microscope

Theoretical models [11] of the 3D imaging formation systems in optical sectioning microscopy assume that the optical systems are free of aberrations. The microscope is characterized by its 3D point spread function (PSF), which is the image of a single point source object through the objective. In these ideal models, the PSF is shift-invariant, which means that the image of a single point source is the same, regardless of its position in the object space.

An ideal, aberration-free objective can be described in terms of the wave-like nature of light. A light wave, of wavelength λ, emitted from a point source in the object plane, is a spherical wave of wavelength λ centered on this point source. A perfect lens transforms a spherical wave into another spherical wave. The image of the point source is a point image. According to Huygens' principle, a spherical wave front consists of a multitude of single point sources, each emitting a spherical wave of wavelength λ [11, 12]. All waves from the same wave front have the same phase origin, and interfere together in the image plane, resulting in a diffraction pattern known as the Airy pattern, consisting of a series of concentric spheres. From this pattern, the lateral resolution limit of a perfect objective with finite numerical aperture can be described by the Rayleigh criterion:

$$r_{latteral} = \frac{0.61\lambda}{n\sin\alpha} = \frac{0.61\lambda}{NA} \tag{1}$$

where n is the refractive index of the medium between the specimen and the objective, α the half cone angle captured by the objective, and λ the emission wavelength. NA is the numerical aperture of the objective. This formula gives the minimum distance that can be separated laterally by an ideal objective of numerical aperture NA, for a given wavelength λ, in two dimensions (Fig. 3).

The two-dimensional analytical formulation of the PSF of an aberration-free microscope [8, 11] can be as follows:

$$h(v) = 2\int_{2}^{1} P(\rho)\, J_0(v\rho)\rho d\rho$$
$$\text{with } \rho = \frac{\sqrt{x^2+y^2}}{a} \text{ and } v = \frac{2\pi NA}{\lambda}\sqrt{x^2+y^2} \tag{2}$$

where P is the circular pupil function of radius a, J_0 the first order Bessel function, λ the emission wavelength and NA the numerical aperture.

Spherical waves issued from the wave front interfere not only in the image plane, but also throughout the 3D space. Consequently, the image of the point source located in the object plane is a three-dimensional diffraction pattern, centered on the conjugate image of the point source located in the image plane.

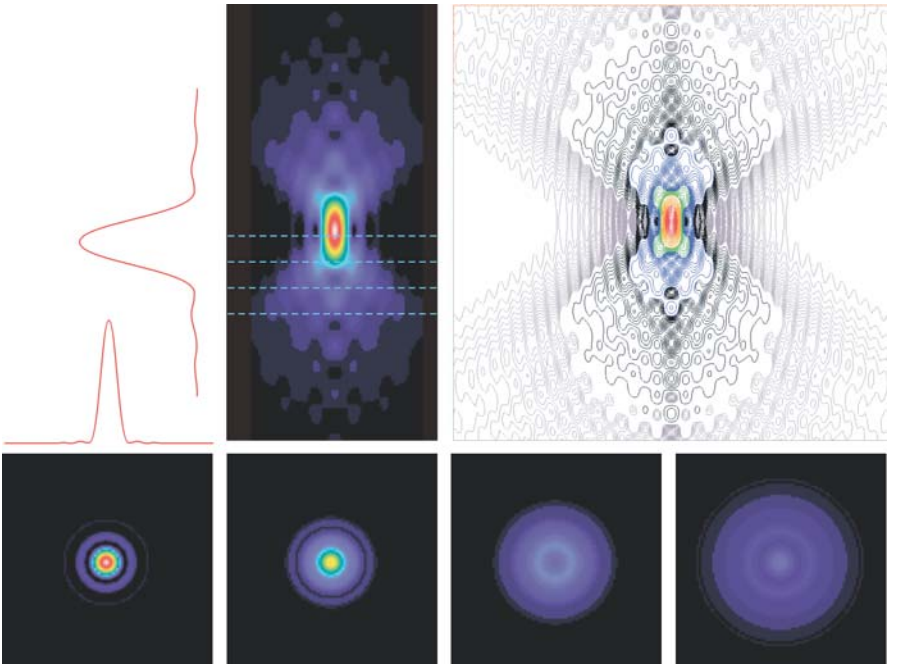

Fig. 3 Diffraction pattern of an ideal, aberration-free objective, in one, two and three dimensions

With a perfect lens, this function is symmetric along the optical axis [11]. The three-dimensional analytical formulation of the PSF for a perfect, ideally corrected and aberration-free objective is given by [6, 13]

$$h(v,u) = 2\int_0^1 P(\rho)\, J_0(v\rho)\, \exp\left(\frac{iu\rho^2}{2}\right)\rho d\rho$$
$$\text{with } u = \frac{8\pi}{\lambda} zn \sin^2(\alpha/2) \tag{3}$$

In the axial direction, intensity distribution is similar in shape to the Airy disk in the lateral direction. As for lateral resolution, axial resolution defines the minimum distance that can be separated in the z-axis. It is described by the distance between the maximum intensity of the central bright region and the first point of minimum intensity along the z-axis, and is given by

$$r_{axial} = \frac{2\lambda n}{NA^2} \tag{4}$$

Unfortunately, this 3D image formation model has been shown to be experimentally inaccurate [13, 14], especially for oil immersion objectives of high

numerical aperture. The next section describes the spherical aberrations that may arise in this case.

2.2 Image Formation in an Oil Immersion Objective with Aberrations

Classical image formation theory, as described above, assumes that the 3D image formation process of a fluorescence microscope is linear and shift-invariant. This implies that a single 3D PSF – the image of a single point source – is sufficient to describe completely image formation throughout the 3D object space. Unfortunately, shift invariance is not always demonstrated, and PSF is all too often a function of the location of the point source in the object space. Most frequently, shift invariance does not apply in the axial direction. Other sources of aberration, including stigmatism, coma and curvature of the field, are negligible and well corrected in high-quality objectives.

Axial shift variance results from the use of objectives under non-optimal conditions. This is unfortunately the case for the observation of biological specimens, particularly in living cell microscopy, in which the emitted light passes through media with different refraction indices. Optical paths differ from the optimal paths for which the objectives were designed, generating spherical aberrations that can severely affect the ideal image of a point source. In general, only the plane position just above a coverslip of a given thickness and refractive index and separated from the objective by immersion oil of a specific thickness and refraction index will produce an aberration-free image, as predicted by classical image formation theory. Any object placed elsewhere within this plane is subject to spherical aberrations.

In practice, it is not easy to carry out microscopy in ideal conditions. For example, the refractive index of a living cell culture is closer to that of water (n=1.33) than to that of immersion oil (n=1.516), and is far from the value for which optics are designed. Consequently, when light is focused deep into a cell well below the coverslip (the point for which the objective is designed), it passes through various layers with different refractive indices, resulting in the generation of spherical aberrations. Spherical aberrations are characterized by axial asymmetry in the shape of the PSF, an increase in the flare of the PSF, and a decrease in its maximal intensity. They decrease both resolution and brightness in wide-field and confocal microscopy. They gradually increase as the focal plane moves deeper into the sample (Fig. 16). They are therefore not seen when recording beads mounted on the coverslip.

Gibson and Lanni [15] proposed a theoretical model taking into account the consequences of the optical path modifications that occur when light rays follow trajectories other than that for which the optics were designed. They calculated the optical path difference (ODP), which is the difference between ideal trajectories and real trajectories, taking into account parameters determining path fluctuation: thickness (*toil*) and refractive index (*noil*) of the immersion oil, thickness (*tc*) and refractive index (*nc*) of the coverslip and the refractive

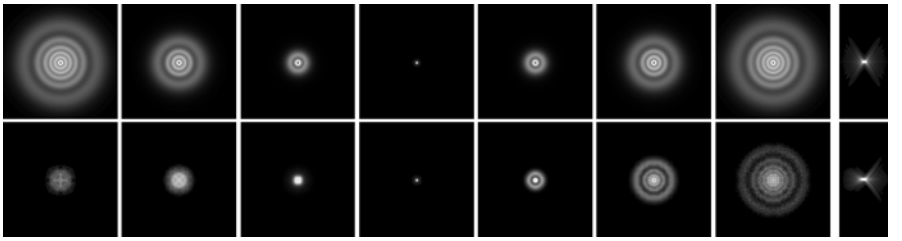

Fig. 4 Comparison of theoretical aberration-free PSF (*top*) and empirical PSF (*bottom*) in the green emission range, for a ×100 1.4 *NA* objective, with an oil immersion refractive index of $n=1.518$

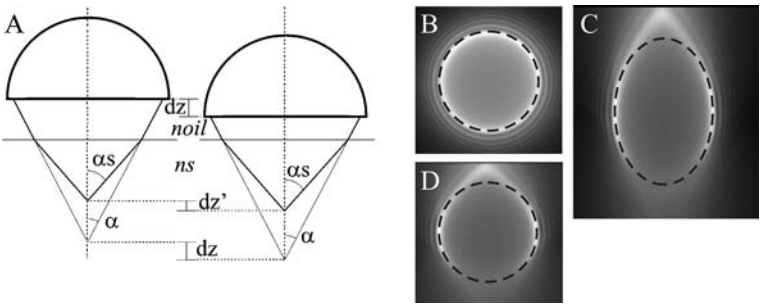

Fig. 5 **A** Axial distance mismatch due to the presence of layers with different refractive indices along the optical path. **B** Lateral section of the bead. **C, D** Observation of a 6 µm fluorescent calibration bead without (C) and with (D) distance calibration

index (*ns*) of the sample. Any deviation of any of these parameters from the optimal values for which the optics were designed will cause spherical aberrations. This model partially describes the spherical aberrations, which can be observed in practice when recording point spread functions from microbeads various distances from the coverslip or when light passes through successive layers with different refractive indices (Fig. 5A).

2.3 Distance Calibration

Another source of distortion that must be taken into account in optical sectioning microscopy is the geometric distortion generated by focusing light through layers with different refractive indices (Fig. 5).

If we ignore the difference between the refractive indices of the immersion oil and the coverslip, the displacement error can be expressed as

$$dz' = \frac{\tan\alpha}{\tan\alpha s}\, dz = \frac{\tan(\arcsin(NA/n))}{\tan(\arcsin(NA/ns))}\, dz \tag{5}$$

This equation quantifies the axial distortions arising from the use of media with different refractive indices between the immersion oil and the sample. This implies that, for the entire light cone to be focused, *NA* must be less than *ns*. For objectives with high numerical apertures, $NA>ns$, and when $ns<n$ (typically when observing living cells with an 1.4 *NA* oil immersion objective) the numerical aperture falls below *ns* and some of the light is lost due to reflection to the medium interface.

This mismatch error may be as high as 3, in the case of living cell (ns=1.33) observed with an oil immersion objective ($noil$=1.516) with a high numerical aperture. This error can be corrected experimentally by attempting to match the immersion medium of the objective with that of the sample (e.g. using a water immersion objective for living samples or by matching the mounting medium and the immersion oil in terms of refractive index for fixed samples). Practically, it is necessary to calibrate the entire acquisition system by imaging fluorescent calibration beads. Figure 5 illustrates the importance of calibrating the microscope. Calibration can be achieved by inputting the measured axial correction factor directly into the acquisition software or, if this is not possible, by interpolating the data once acquired. This step is crucial for acquisitions of three-dimensional data with optical sectioning. Sampling errors can cause major problems in deconvolution processes using a theoretical PSF, in which the details of sampling must be precisely known. More generally, without this correction step, acquisitions can be achieved either by oversampling (when $ns<n$) or by downsampling (when $ns>n$). However, oversampling may lead to photobleaching and damage to the cell whereas downsampling may result in a loss of information.

2.4 Determination of the Point Spread Function

The PSF describes the response of the microscope, for each point of the sample imaged. This information is required for most deconvolution algorithms because it describes the way in which the objective distorts the image during the acquisition process. Assuming that the image formation process is linear and shift-invariant (this point will be discussed later), a single function completely describes the functioning of the instrument at any point in the specimen. The accuracy and quality of the PSF are essential to ensure the correct performance of any deconvolution algorithm. Noise, incorrect estimates of aberrations and incorrect scaling of the PSF may cause major artifacts in the restored image.

The PSF may be calculated theoretically or measured empirically. There are advantages and disadvantages to both methods. In addition to simplifying the process by avoiding the need for time-consuming PSF extraction, the main advantage of theoretical PSF calculation is the absence of noise. It is therefore possible to determine, with similar levels of accuracy, the 3D contributions of the PSF within and outside the focal plane, at a distance at which detectors are not sensitive to capture any signal above the noise. Nevertheless, there are many

reasons for preferring an empirical model. First, although good theoretical PSF models exist (see above), they apply only to perfect lenses and well defined and calibrated optical paths, which are, of course, never found in practice. Small variations in the regularity of the lens may change the shape of the PSF in ways that cannot be predicted by theoretical models. Second, some spherical aberrations are very difficult to predict theoretically. Any discrepancy between the theoretically estimated PSF and the actual PSF of a microscope decrease the efficiency of the deconvolution and may result in artifacts in the results.

Although theoretical estimates cannot provide an exact measure of the real PSF of objectives, they may nonetheless be of value for estimating expected values in ideal experimental conditions. This requires precise knowledge of the microscope setup and the use of a theoretical PSF generator, taking into account the spherical aberration primarily due to the mismatch of refractive indices along the optical path, as described above. This model requires precise knowledge of the numerical aperture of the microscope, the objective to object path length, the emission wavelength, the refractive index of both immersion and sample media and the thickness of the coverslip. In addition, (x, y, z) sampling is also required to represent the final result in a discrete manner. Sampling identical to that for acquisition is used, in general, so that the extracted PSF can be used directly in deconvolution or compared with the measured PSF. If a theoretical PSF-based deconvolution is performed on acquired data sets, then absolute calibration of the microscope optics must be carried out first (see previous section).

For accurate determination of the microscope's PSF, it is advisable to measure the PSF under the same conditions as used for the sample itself. Each objective is unique, and any variation in the regularity of the lens may affect PSF shape, particularly for immersion objectives with a high *NA*. Moreover, PSF measurement can detect problems in the microscope setup that may not be evident when observing complex biological samples. There are many possible sources of problems, including oil mismatch, objective defect, vibrations from the heating system or CCD cooling, and unexpected changes in the properties of the oil when working at different temperatures (e.g. room temperature and 37 °C). In the face of these potential sources of signal degradation, it is strongly recommended that the microscope's optical properties, stability and reproducibility should be checked with microbead samples (Fig. 6).

PSF can be measured experimentally in a simple manner involving the acquisition of images of subresolution fluorescent beads. These microbeads, commercially available as a concentrated solution, are used to represent a point source for evaluation of the system. The smallest beads possible should be used in theory, but small beads are weaker in intensity and bleach more rapidly. In practice, beads with a diameter less than half the resolution are used: beads of 0.15 μm in diameter, from Molecular Probes Inc., for a 1.4 *NA* oil immersion objective with a lateral resolution of 0.4 μm at an emission wavelength of 500 nm. Beads are diluted to isolate each PSF without overlap, and are dried onto the coverslip. The coverslip is then reversed, mounted in the same medium as used

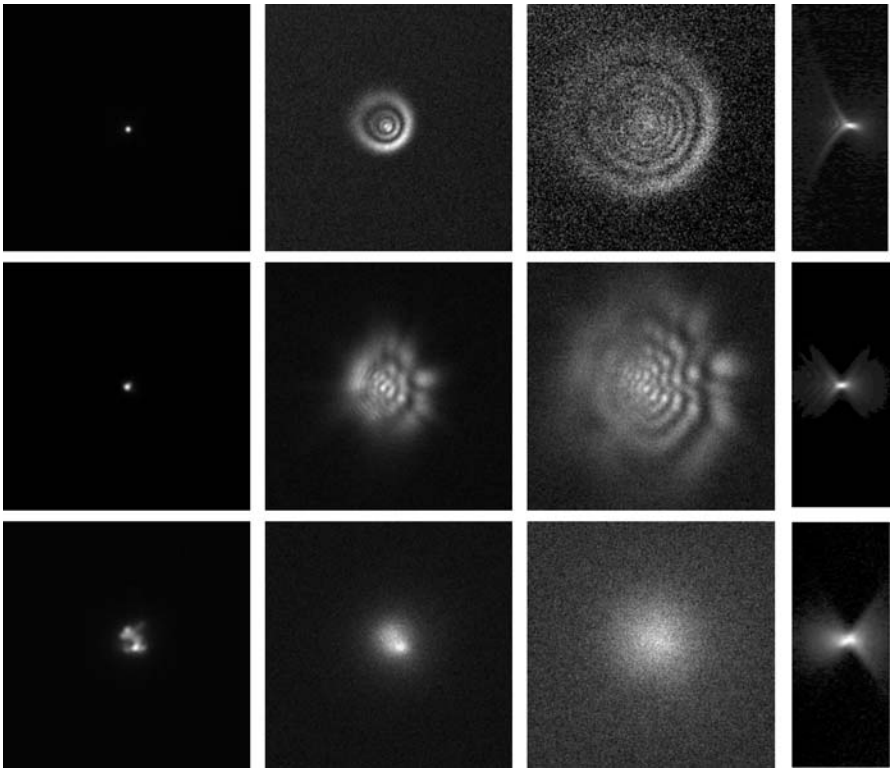

Fig. 6 Examples of artifacts: optical problem (*top*), oil mixing (*middle*) and vibrations (*bottom*)

to embed the sample, and attached firmly to the slide with nail polish to ensure that the specimen remains stable during the acquisition. Optical sections of bead samples must be achieved, using an optimal sampling method, compatible with optic axial resolution and deconvolution, as for the sample itself (see below). An image stack can then be collected, adjusting excitation and exposure time parameters to maximize the dynamics in the center of the bead without saturating the signal, and to prevent bleaching. To increase the signal-to-noise ratio of the image, especially in the out-of-focus regions in which signal intensity is weak, it is recommended to average acquisitions of multiple beads. The acquisition protocol can be facilitated by using the same bead for the averaging, keeping bleaching minimal. The signal-to-noise ratio can be increased significantly by applying circular averaging with respect to the optical axis, if, of course, the original bead acquisitions show the symmetry predicted by the theory (Fig. 7).

If possible, all conditions resulting in a change in PSF shape should be characterized. Identified sources of changes in optical properties include (1) emission wavelength, (2) axial distance to the coverslip and (3) refractive indices.

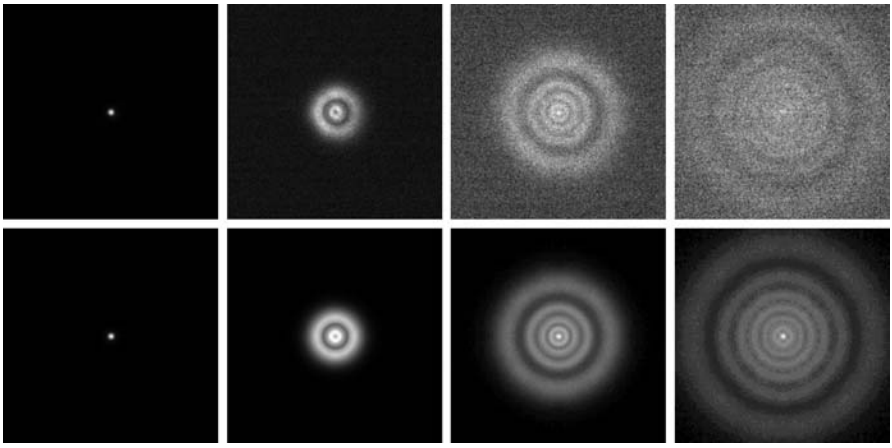

Fig. 7 Experimental PSF extraction: raw data (*top*), and data after bead averaging and circular symmetry processing (*bottom*)

1. As PSF is a function of emission wavelength [16], the objective must be characterized with different color beads. Multicolor beads (Tetraspec, Molecular Probes Inc.), conjugated with four different fluorescent probes, provide a broad range of types of emitted light (UV, green, red and IR), facilitating spectral characterization of the objective. Moreover, these measurements can be used to check, and even to correct after acquisition, the non-apochromatism of the lens (Fig. 8).
2. As described above, spherical aberrations break shift invariance in the axial direction. Consequently, if thick objects need to be observed in their entirety (more than about 20 μm), or if objects located far from the coverslip are to be observed, it is advisable to characterize the microscope's PSF at various z levels. This can be done theoretically, or experimentally by recording flu-

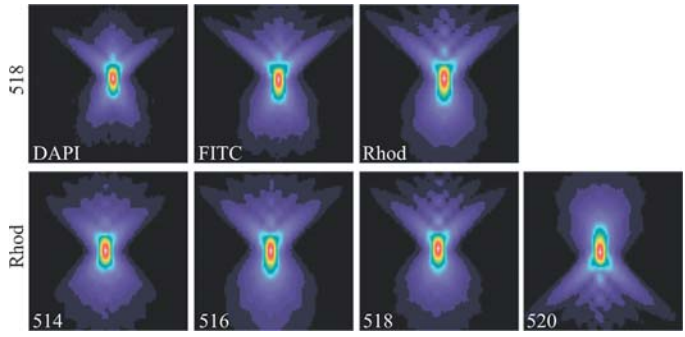

Fig. 8 *Top*: PSF for Dapi, GFP and rhodamine wavelengths, using an oil with a refractive index of 1.518. *Bottom*: PSF for the rhodamine wavelength, using oils with refractive indices of 1.514, 1.516, 1.518 and 1.520

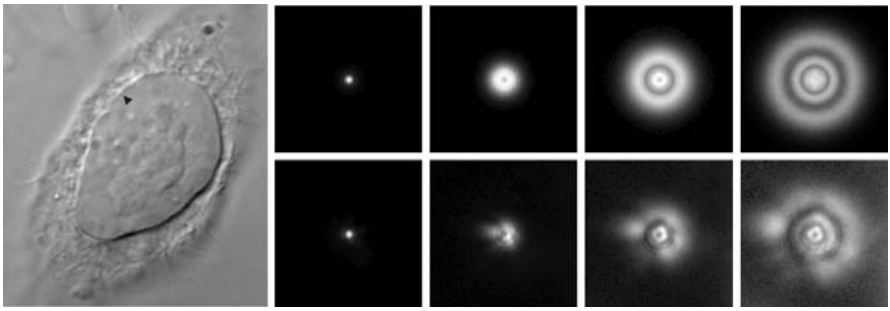

Fig. 9 Distortion of a PSF due to the natural fluctuation of local refractive indices. Fluorescent beads were injected into a cell before fixation. *Top*: Experimental PSF determined in the absence of a cell. *Bottom*: Distorted PSF determined from a bead within a cell. *Left*: DIC image of the cell, showing local refractive index variations; the *black arrow* indicates the location of the bead

orescent microbeads lying on the surfaces of gels of a given thickness and refractive index.

3. Ideally, PSF should be measured under the same conditions as the specimen itself. In practical terms, this implies that beads should be observed after injection into the specimen, which is generally not possible. Neither theory nor experimental methods can predict the change in PSF caused by the passage of light through a heterogeneous medium of unknown refractive index. Estimation of the local refractive index can be achieved by acquiring pre-DIC images on the sample. Its knowledge allows to model the PSF distortions for each point of the whole volume, using ray-tracing techniques [17], without the need to inject microbeads into the cell. This local information is of value because it makes possible to perform deconvolution with precise knowledge of the PSF. However, under such circumstances, the PSF cannot be assumed to be shift-invariant, limiting deconvolution due to the extremely large amount of computation time required (Fig. 9).

This illustrates the difficulties and limitations of the PSF extraction process for the observation of biological specimens. Neither theory nor experimental determinations can precisely predict the PSF that should be used for the deconvolution of a complex biological sample. Empirical measurements are clearly the most appropriate method, but comparison of the values obtained with those predicted by the theoretical model can help to solve problems in the optical setup. One good solution would be to fit an analytical model to the experimental acquisition, to make the best use of both approaches. One recent study adopted such a method [18] recovering iteratively the theoretical shape of the pupil function, including phase information, from bead acquisitions. This made it possible to model aberrations causing axial asymmetry. However, this method cannot be used to overcome problems with shift invariance, an essential requirement of deconvolution algorithms that often does not apply completely in practice.

Thus, the image formation process in optical sectioning microscopy differs from classical image formation theory. Variations in refractive index along the optical path and lens imperfections are the main causes of spherical aberrations. These aberrations are difficult to describe perfectly in theoretically terms and cause a breakdown of axial symmetry and shift invariance properties. Shift invariance property is in some cases very useful for highly simplified mathematical descriptions of the image formation process, mostly for deconvolution (see below for more details). Shift invariance can be assumed to apply in a certain range of thickness, particularly if the optical path is close to the ideal case for which the optics were designed. It is therefore important to characterize experimentally and to adjust the optical setup before routine acquisition and deconvolution, to stick as closely as possible to the ideal case. This can be achieved by selecting the most appropriate objective with the highest possible quality and by adjusting the refractive index layers along the optical path. As each lens is unique, different objectives must be tested and the objective providing the PSF closest to the theoretical value should be used. In practice, it is a good idea to characterize the microscope using the coverslip and to assume axial shift invariance in a thickness range of 10 to 15 μm. This makes it possible to observe a cell monolayer by optical sectioning deconvolution microscopy. If structures deeper within the cells are to be investigated, then the microscope should be characterized at a z distance close to the volume of interest. In all cases, the z-calibration procedure described in the previous section must always be carried out first.

3 Image Acquisition

In optical sectioning microscopy, a three-dimensional stack of two-dimensional images is recorded. Each 2D image corresponds to object acquisition at one focal plane position.

3.1 Sampling

As acquisitions are digital, sampling constraints must be checked to maximize the resolution of the objective. The Nyquist theorem states that for a frequency-limited system, which is the case for any numerical aperture-limited objective with a given resolution limit r, a sampling Δ of half of the resolution is sufficient for the digital recording of the entire signal with no loss of information. For 3D microscopy, the theorem can be expressed for the lateral and axial directions as follows:

$$\Delta_{xy} \leq \frac{r_{xy}}{2} \text{ and } \Delta_z \leq \frac{r_z}{2} \tag{6}$$

where r_{xy} and r_z denote the lateral and the axial resolutions, and Δ_{xy} and Δ_z the lateral and axial samplings. In other words, images must be sampled using at least two points per resolvable element.

In wide-field microscopy, lateral sampling is achieved by the CCD chip and is a function of the CCD pixel size P_S, camera binning b, and objective magnification M, as follows:

$$\Delta_{xy} = \frac{P_S b}{M} \tag{7}$$

By incorporating the lateral resolution equation (Eq. 1) into Eq. 7, the lateral sampling criterion can be rewritten as

$$\frac{NA}{M} \leq \frac{0.61\lambda}{2P_S b} \tag{8}$$

This relationship provides the ideal objective range, for a microscope setup with a given CCD chip, for checking the Nyquist theorem and ensuring compatibility with deconvolution.

For scanning confocal microscopy, lateral sampling is subject to no such constraints and may be ideally adjusted with the zoom command to satisfy the Nyquist theorem. For both wide-field and confocal microscopes, axial sampling must also be adjusted by selecting an appropriate plane spacing distance.

However, this criterion produces the minimum necessary sampling step for obtaining a discrete signal from a real continuous signal. In practice, it is recommended to slightly oversample the signal to optimize separation of the high-frequency noise from the signal itself. Ideally, it is good practice to sample three points per resolvable element. However, practical aspects must be taken into account, particularly when observing living samples. Oversampling increases the number of images required for a given acquisition volume. This results in a significant increase in phototoxicity, acquisition time and photobleaching, each of which may cause artifacts in optical sectioning microscopy combined with deconvolution, and must be minimized:

- Phototoxicity results from prolonged illumination when observing living biological samples. It results in irreversible light-induced damage, mainly due to emission of free radicals, which may lead to changes in the behavior of the living sample, and even to the death of the sample.
- Increasing the acquisition time per time point for living samples may generate artifacts in the deconvolution process. Given that the goal of deconvolution is to "reassign" the light to its original place, the objects must not move within the resolution limit of the microscope during the optical sectioning acquisition process.
- Fluorescence is produced by a cycle in which an electron of a chromophore is excited from its ground state to an excited state, and then relaxes back to

the ground state, resulting in the emission of a photon. Instead of displaying the expected fluorescence relaxation, the excited state can undergo a variety of photochemical reactions that destroy fluorescence. This fluorophore destruction is called photobleaching, regardless of the underlying mechanism responsible. The repeated and prolonged exposures needed to acquire multidimensional data by optical sectioning microscopy result in the continuous loss of cell fluorescence. This loss of fluorescence, if arising during a single stack acquisition, may result in the incorrect estimation of the real light intensity distribution. Consequently, the restoration step may lead to the artifactual reassignment of light. This can be prevented by carrying out a pre-processing step to correct z-bleaching [19]. Undesirable fluctuations in illumination, such as lamp jittering, must also be corrected. If bleaching occurs gradually during time-lapse acquisition, it results in a progressive decrease in signal-to-noise ratio from stack to stack. As noise limits the efficiency of the deconvolution process, this may result in unstable data that are non-reproducible from one stack to another.

Another important criterion is sampling volume: ideally, all the emitted light should be collected for reassignment to its original location. In wide-field microscopy, the light emission cone extends to a few microns above and below the emission plane. This implies that a few microns above and below the peripheral planes containing the object should be acquired so that all the out-of-focus information can be taken into account in the deconvolution process. This is not feasible practically, resulting in a deconvolution process that is less efficient in the peripheral planes than in the middle planes. This "missing information" problem is even greater if only the subvolumes of interest are acquired. In such cases, corresponding mostly to living-cell microscopy in which rapid processes must be acquired over a short period of time, the number of planes must decrease with the observation area. This results in some of the signal not being captured and therefore not being taken into account for deconvolution. This limitation can be partially overcome by means of an intermediate approach involving the use of optical sections with a varying interplane distance [20]: small enough in the volume of interest for checking of the sampling criterion, but larger further away. Unfortunately, this acquisition protocol is not compatible with the high-speed acquisition of the streaming mode described below (Fig. 10).

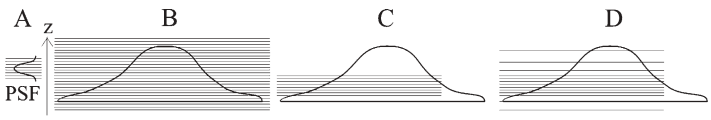

Fig. 10 **A** PSF and optimal sampling (sampling criterion). **B** Ideal full-object sampling. **C** Practical subobject sampling, in which only the volume of interest is acquired, to reduce exposure time. **D** Intermediate object sampling using varying steps, in which only some of the out-of-focus information is collected

3.2 Optical Setup

In this section, wide-field deconvolution microscopy will be treated as an alternative to confocal microscopy because it is more flexible, and under some circumstances, more appropriate. Despite the use of common equipment, fixed and living sample acquisition protocols will be treated separately because the different constraints associated with these protocols ultimately end up leading to individual setups.

A deconvolution microscope may be assembled from individual components or purchased as an integrated solution. Although time-consuming, assembly offers a much higher level of flexibility and is generally less expensive than an integrated solution. This option makes it possible to build up a system to fulfill precisely the requirements of the research group, whereas integrated systems provide a more general solution. Moreover, there is continual progress in imaging techniques, optical devices, detectors, motorization and other elements, and a flexible "custom-assembled" setup makes it much easier to update the system. The essential components of a deconvolution microscope include: a standard microscope mounted on an anti-vibration table, a microstepping motor to control the focus, a fluorescence illumination device – including excitation filter, dichroic mirror, emission filter and shutter elements – a cooled high-resolution CCD camera and software for optimizing the control and synchronization of all these elements. It may be useful to maintain control of the bright-field transmission mode, to facilitate localization of the tagged fluorescent proteins within the cell. The main differences between fixed and living sample experiments, regardless of the temperature and atmospheric controls for living cells, are the fluorescence setup and the way in which multicolor images are collected.

3.2.1 Fluorescence

In fixed-sample experiments, standard single-color filter blocks are used in combination with white-light illumination and a shutter. Multilabels are then acquired, color-stack by color-stack, by simply changing the dichroic mirror block device from one position to another. This process makes use of the high intensity of the standard equipment, provided by single dichroic filter blocks. This equipment is more efficient and specific than multicolor dichroic filter blocks. With the standard system, only the dichroic block, the shutter and the z-motor have to be motorized. If a standard mechanical shutter is used, it can be left open during stack collection for faster acquisition.

For living-cell microscopy, multilabeling acquisition is constrained by the fact that objects are likely to move during the collection of stacks. Multicolor images must therefore be acquired as rapidly as possible, and the sequential stack-color mode described above is inappropriate. There is a single solution to this problem: using a multiband pass dichroic mirror and dissociating

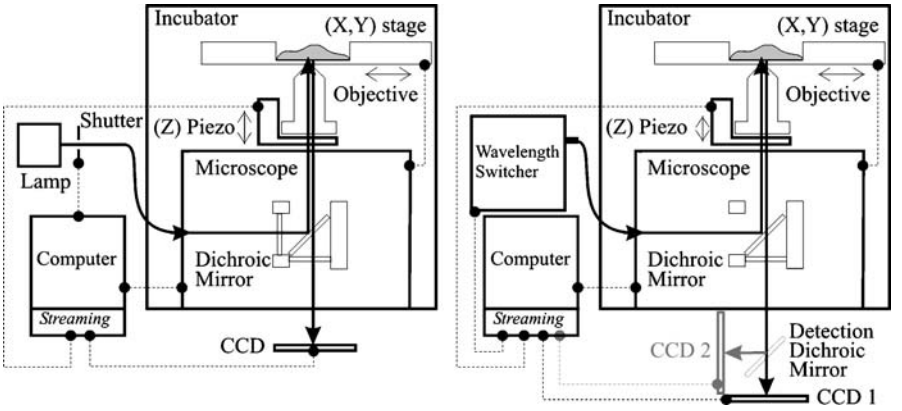

Fig. 11 Typical optical setup of a fast multidimensional microscope for fixed (*left*) and living (*right*) cell observation. For fixed-sample acquisition, image stacks are acquired sequentially, one color at a time. Single dichroic mirrors are used and exchanged to switch between colors. For living-cell microscopy, the dichroic mirror is fixed and contains a multiband filter. In sequential mode, for each focal position, excitation wavelengths are changed with a fast wavelength switcher, and only one CCD camera is needed. In simultaneous mode, several CCD cameras are used in combination with an adapted detection dichroic mirror

excitation and emission. For each plane, different wavelengths are sequentially or simultaneously acquired:

- In the sequential mode, excitation wavelengths for a given observation succeed each other. Emission wavelength can be fixed with a multi-band emission filter or synchronized with excitation part, using single-band emission filters.
- In the simultaneous mode, multi-excitation band-pass filters are used to excite all the fluorophores at the same time. Dichroic emission beam splitters are used at the detection level to separate emission wavelengths and to record multicolor images simultaneously. Images are recorded either by splitting the image fields on a single camera or by using several cameras (Fig. 11).

3.2.2 Detection

The detector and the means of controlling it are of key importance for high-speed acquisitions. With the ever-increasing sensitivity and speed of detectors, digital cameras make it possible to continually increase the speed of recording of weak signals. Up to 100 frames per second can be recorded, depending on the type of camera and the size of the region observed. An understanding of the acquisition process depends on knowledge of the workings of CCD cameras, the details of which can be found elsewhere [12].

A CCD chip consists of an array of small isolated photodiodes. The acquisition process consists of three steps: (i) charge integration, (ii) charge transfer

and (iii) read-out. During charge integration, photons are captured by each individual diode during a given period of integration, also known as the exposure time. Photon absorption results in the formation of electron-hole pairs, which move toward their respective electrodes, and are accumulated in a potential well. During charge transfer, the charges stored in each pixel are shifted to a serial readout register, by means of a cascade of synchronized parallel and serial shifts. Once in the serial register, the readout process starts. Packets of electrons are sequentially read, amplified and converted into an analog signal proportional to the number of stored charges in each pixel. Finally, this raster scan of the CCD chip is converted into a digital signal and loaded into the memory of the computer via a frame grabber.

In a standard full-frame CCD chip, three steps must be performed sequentially before the next image acquisition process begins. For frame transfer and interline transfer CCD technologies, the presence of an intermediate buffer makes it possible to discharge the potential well rapidly by rapid parallel shift. Once shifted to the readout buffer, the next acquisition sequence can start, continuing in parallel with the readout process.

Neighboring pixels can be grouped together to form a larger "super-pixel", and this process can be used to increase the acquisition rate. This technique, known as binning, has two positive consequences: first, the signal-to-noise ratio is increased by increasing the absorption surface, and second, the number of pixels transferred is reduced. Unfortunately, binning increases the pixel size of the image, thereby reducing sampling frequency. Consequently, the constraints imposed by the sampling criterion (see above) may not be fulfilled, possibly decreasing image quality and resulting in images incompatible with the deconvolution process. In practical terms, the same tradeoff is always made between speed, sensitivity and resolution (Fig. 12).

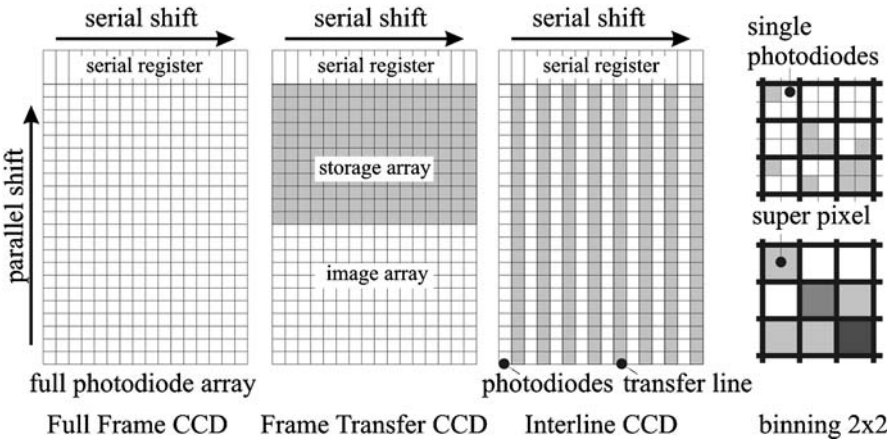

Fig. 12 CCD architecture of full frame, frame transfer and interline CCD and details of the binning mode

3.2.3 Streaming

Image acquisition with frame and interline transfer CCD cameras can clearly be optimized by making the integration and read-out processes function in parallel. This maximizes acquisition speed, with image stacks collected in RAM at maximum speed. This operating mode, called streaming, is optimal if the readout time (TR) is shorter than the exposure time (TE). In this case, acquisition time depends only on exposure time. In practice, once the exposure time is determined from single images produced with a sufficiently high signal-to-noise ratio, the acquisition region should be adjusted with respect to the camera readout speed. For rapid living-cell microscopy, binning and streaming are often combined (Fig. 13).

In multidimensional microscopy, focus and wavelength changer devices must be controlled between image acquisitions. To maintain streaming efficiency, z-streaming and lambda-streaming have been developed for high-speed multicolor stack collections. During this process, the z-position and/or excitation wavelength is changed during the shift register step in streaming mode. This solution requires high-speed devices responding within a few milliseconds, such as piezo-electric focus devices, DG4 or monochromator illumination devices.

Nevertheless, during streaming, acquisition parameters such as exposure time and plane distance cannot be changed. This constrains exposure time, which must be identical for each color during a fast multicolor acquisition, and precludes the use of a variable z-step as described earlier.

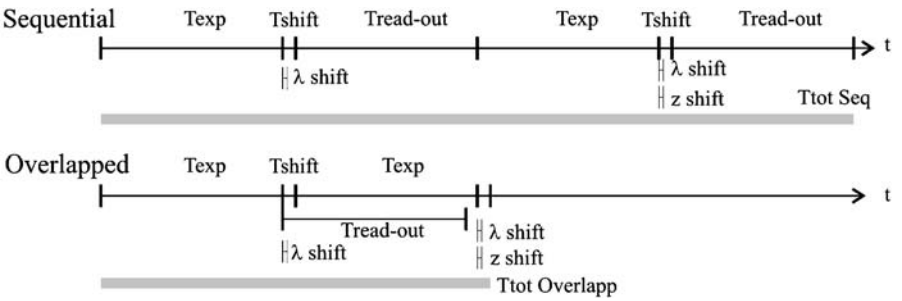

Fig. 13 Time-course diagrams of sequential and overlapping (streaming) acquisition modes

4 Deconvolution

Deconvolution is a computerized inversion method for restoring an image distorted during the image formation process, based on prior knowledge of the degradation phenomenon. In microscopy, the goal is to reassign the optical blur to its original position and to reduce statistical noise. Image restoration belongs

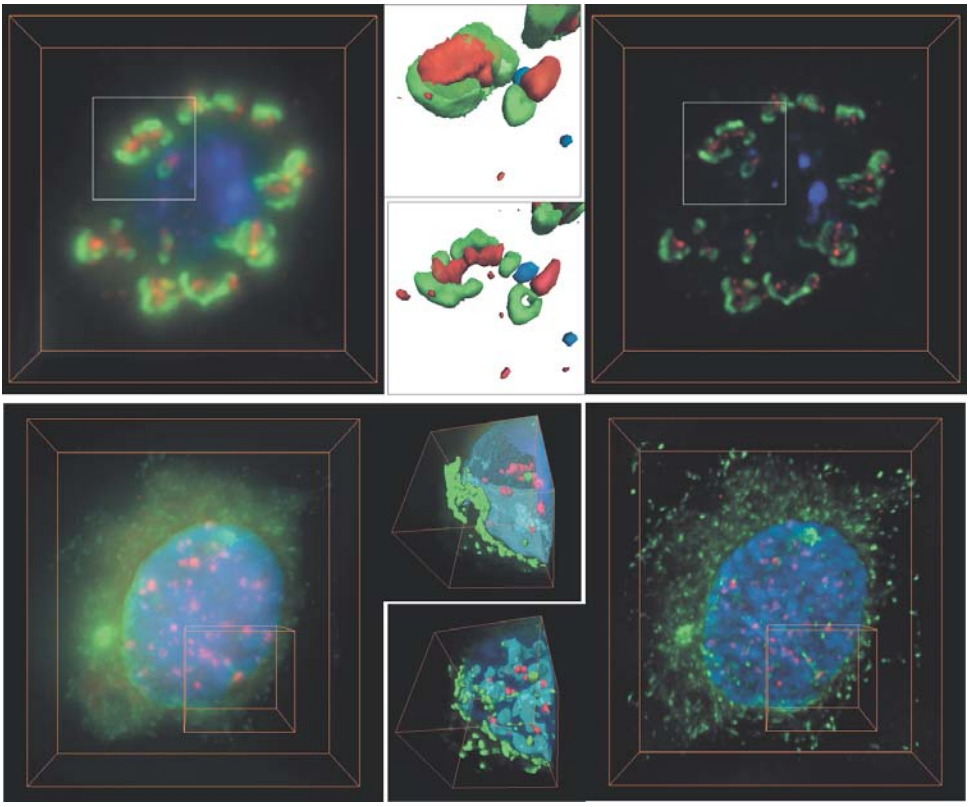

Fig. 14 *Top*: Volume rendering by maximum intensity projection (*left and right*) and surface rendering (*middle*) of drosophila S2 cells stained for two different antigens localized to the Golgi apparatus. Golgi in Drosophila cells consists of several independent units dispersed into the cytoplasm. The deconvolution clearly reveals that these antigens are localized to different but closely apposed regions of Golgi units. Courtesy of I. Kouranti and A. Echard, Institut Curie. *Bottom*: Volume rendering by maximum intensity projection (*left and right*) and surface rendering (*middle*) of HeLa cells labeled for $p150^{Glued}$ (*green*), centromeres (CREST, *red*) and DNA (DAPI, *blue*). Initial data (*left*), restored data (*right*) and zoom on the surface rendering (*middle*) to illustrate the gain of resolution provided by the deconvolution and its contribution to the segmentation process. This prophase cell displays the classic pattern of labeling of microtubule plus ends by p150. After deconvolution, centromeric regions from one pair are resolved into two contiguous spherical regions and the DNA condensing events occurring in the prophase nucleus are visible in the segmented data. Nevertheless, the pattern corresponding to bright green dashes, easily visible in the volume rendering image, displays segmentation into ball-like structures. This illustrates the limitation of biological object segmentation, which cannot always be resolved, even with the best deconvolution methods available. Courtesy of F. Cordelières, Institut Curie

to the ill-posed problem category and does not generate a single solution. The result is an estimate of the object $\hat{o}$ that is closer to the observed object o than the acquired image i. In addition to improving visualization of the details of the image, deconvolution also facilitates segmentation and analysis, as illustrated in Fig. 14.

In the next section we will provide some mathematical definitions of the problem and will then go on to detail the most commonly used algorithms.

4.1 Degradation Model and Mathematical Formalism

The degradation process can be modeled as an operator H, which, together with the noise N, operates on an input image o to produce a distorted image i. Digital deconvolution is a mathematical process that computes an object's approximation $\hat{o}$, given the acquired image i, knowledge of the degradation model H, and the noise N. In general, knowledge of N is limited to knowledge of its statistical nature. In optical microscopy, degradation is mostly due to the optical blur generated by out-of-focus contributions of the object in the focal plane, and statistical noise. Assuming that noise follows a Poisson distribution (see above), it can be approximated by a Gaussian additive distribution for the purposes of simplification.

4.1.1 Continuous Formulation

In the case of continuous functions, the general relationship between input and output can be expressed as follows:

$$i(x, y, z) = N(\iiint o(x', y', z')\, h(x, y, z, x', y', z')\, dx'\, dy'\, dz') \tag{9}$$

where i is the acquired image, o the object acquired, h the PSF and N the noise. Assuming linearity and shift invariance in the image formation process (under certain conditions detailed above), the triple integral can be simplified to

$$i(x, y, z) = N(\iiint o(x', y', z')\, h(x - x', y - y', z - z')\, dx'\, dy'\, dz') \tag{10}$$

which is a standard 3D convolution integral that can be written as

$$i(x, y, z) = N(h(x, y, z) \otimes o(x, y, z)) \tag{11}$$

This equation describes, by means of a simple mathematical convolution operator, the way in which the acquired object o is degraded during the image formation process: first by being blurred with the instrument function h and secondly by noise degradation N. The convolution can be made in the Fourier domain, making it possible to use the mathematical property that a convolu-

tion in the spatial domain becomes a point-by-point multiplication in the Fourier domain

$$FFF\{h(x, y, z) \otimes o(x, y, z)\} = H(u, v, w)\, O(u, v, w) \tag{12}$$

where italic capital letters represent the Fourier transformations of the corresponding lower-case variables, and *FFF*{} the 3D Fourier transform operator. The Fourier transformation of the PSF, *H*, is called the optical transfer function (OTF).

4.1.2 Discrete Formulation

The discrete mathematical formulation of image formation is as follows:

$$i_m = N(\sum_l h_{l-m}\, o_l) = N(a_m) \tag{13}$$

This equation is referred to as the classical imaging equation, from which many iterative algorithms are derived, with a_m is introduced as the noise-free image. At any point *m* of coordinates $m=(x, y, z)$ in three dimensions, the acquired image for the point i_m is equal to the sum of contributions of the entire observed object *o*, weighted by the blurring function *h,* which is the microscope's PSF. The noise *N* associated with each point is independent of the image formation system.

4.1.3 Matrix Formulation

The classical imaging equation can also be expressed in matrix notation as follows:

$$\mathbf{i} = N(\mathbf{Ho}) \tag{14}$$

where **i, o** and **n** are one-dimensional matrices of size M, obtained by concatenation of their respective rows. **H** is a block circulant blurring matrix of size M×M. This notation can be used for the formulation of a class of well-known direct restoration algorithms.

In fluorescence microscopy, the convolution operator implies a linear and shift-invariant point spread function *h*. Although we showed earlier that this assumption does not hold true in all cases, this approximation will be assumed in the future because it simplifies computation of the solution.

An obvious way to reverse the convolution equation in the Fourier domain and to recover *O* given *I* and *H* would be to divide *I* by *H*. Unfortunately, in the presence of noise, the Fourier transformation of the PSF has a finite support and falls rapidly to zero because of the lack of resolution. This results in divisions by very small or zero values, making it impossible to divide *I* by *H*. In addition, noise is amplified during division, leading to the generation of ma-

jor artifacts. Such problems are called ill-posed or ill-conditioned problems, for which a unique solution of the object cannot be directly recovered without additional knowledge. All restoration methods, whether direct or iterative, aim to generate an estimate of the object o, denoted $\hat{o}$, generally by minimizing a function or criterion.

There are various families of deconvolution algorithms, each with its own advantages and limitations. These algorithms are powerful for the processing of images with known properties (e.g. for a given signal-to-noise range), but produce poor results in other cases. Unfortunately, the algorithms providing the best results with simulated data do not necessarily provide the best results with real acquired data. No best method has yet been identified in practical terms. We will now describe the algorithms most frequently used in published studies, providing results obtained with commercially available packages.

4.2 Wiener Filtering

This restoration technique involves estimating $\hat{\mathbf{o}}$, such that $\mathbf{H}\hat{\mathbf{o}}$ approximates $\mathbf{i}$ in the least squares sense [21]. In the absence of constraint, this is achieved by finding the value of $\hat{\mathbf{o}}$ that minimizes $\|\mathbf{i} - \mathbf{H}\hat{\mathbf{o}}\|^2 - \|\mathbf{n}\|^2$. Assuming that the norm of the noise is small, this is equivalent to minimizing the function

$$\mathbf{\Phi}(\hat{\mathbf{o}}) = \|\mathbf{i} - \mathbf{H}\hat{\mathbf{o}}\|^2 \tag{15}$$

with respect to $\hat{\mathbf{o}}$. The minimization of $\mathbf{\Phi}$ is straightforward and is achieved by setting to the zero vector the derivative of $\mathbf{\Phi}$ with respect to $\hat{\mathbf{o}}$:

$$\frac{\partial \mathbf{\Phi}(\hat{\mathbf{o}})}{\partial(\hat{\mathbf{o}})} = \mathbf{0} \tag{16}$$

The solution is the classical unconstrained inverted equation

$$\hat{\mathbf{o}} = \frac{\mathbf{H}^{\mathrm{T}}\mathbf{i}}{\mathbf{H}^{\mathrm{T}}\mathbf{H}} \tag{17}$$

which has been reported to be unsolvable in practice, mainly because of the non-existence of $\mathbf{H}$'s inverse.

A more flexible approach involves adding constraints by minimizing functions of the form $\|\mathbf{Q}\hat{\mathbf{o}}\|^2$, where $\mathbf{Q}$ is a linear operator on $\mathbf{o}$, subject to the constraint

$$\|\mathbf{i} - \mathbf{H}\hat{\mathbf{o}}\|^2 = \|\mathbf{n}\|^2 \tag{18}$$

with $\|\mathbf{i} - \mathbf{H}\hat{\mathbf{o}}\|^2 = \|\mathbf{i} - \mathbf{H}\hat{\mathbf{o}}\|^{\mathrm{T}}(\mathbf{i} - \mathbf{H}\hat{\mathbf{o}})$ and $\|\mathbf{n}\|^2 = \mathbf{n}^{\mathrm{T}}\mathbf{n}$. This minimization problem can be resolved with Lagrange multipliers, by minimizing the criterion function

$$\mathbf{\Phi}(\hat{\mathbf{o}}) = \|\mathbf{i} - \mathbf{H}\hat{\mathbf{o}}\|^2 + \alpha\|\mathbf{Q}\hat{\mathbf{o}}\|^2 \tag{19}$$

where α, the Lagrange multiplier, is a regularization parameter. Again, $\mathbf{\Phi}$ is minimized by its derivation with respect to $\hat{\mathbf{o}}$, and setting the result to the zero vector, which gives

$$\hat{\mathbf{o}} = \frac{\mathbf{H}^{\mathrm{T}}\mathbf{i}}{\mathbf{H}^{\mathrm{T}}\mathbf{H} + \eta\mathbf{Q}^{\mathrm{T}}\mathbf{Q}} \tag{20}$$

with η=1/α. This equation, also known as the Tikhonov-Miller solution, can also be derived from Bayesian theory. Approaches to the determination of an optimal value of η will be discussed in the statistical approach to restoration methods (see below).

From Eq. (20), the well known Wiener invert filter [21] can be obtained and expressed in the Fourier space as follows:

$$\hat{O}(u, v, w) = \frac{H^{*}(u, v, w)}{|H(u, v, w)|^2 + K} I(u, v, w) \tag{21}$$

where H^* is the complex conjugate of H and $|H(u,v,w)|2=H^*(u,v,w)\ H(u,v,w)$. In the Wiener invert filter, η is set to 1 and K is defined as P_n/P_o, where P_n and P_o represent the power spectra of the noise and the object, respectively. In practice, P_n and P_o are unknown and K is a constant, in the range 0.001 to 0.1 [23].

This direct restoration method is straightforward and requires only modest computation power. However, it is sensitive to PSF, and small errors in the estimation of PSF may result in major artifacts. This algorithm is often used in practice as a first approximation in iterative procedures. The iterative approaches presented below, although more demanding in terms of computation power, have been shown to be less sensitive to errors and to generate more stable estimates of o.

4.3 Nearest Neighbors

This technique does not use all the out-of-focus information, but does use that contained in the two adjacent planes above and below the plane of interest: the nearest neighbors [22, 23]. This method is based on the principle that these two planes make the most substantial contribution to the central plane. Thus, only the contributions of these two planes are taken into account for correction of the central plane, with other out-of-focus contributions ignored. The general convolution relationship between the acquired image i and the object o can be simplified and rewritten for the k-th plane as a function of the information constrained in the adjacent (k-1)-th and (k+1)-th planes:

$$i_{\mathrm{k}} = o_{\mathrm{k}} \otimes h_0 + o_{\mathrm{k-1}} \otimes h_{-1} + o_{\mathrm{k+1}} \otimes h_{+1} \tag{22}$$

where indices denote the plane number for i and o, and the plane distance relative to the focal plane h_0 for h. Assuming that $o_{\mathrm{k}\pm1} \approx i_{\mathrm{k}\pm1}$ and ignoring the

difference between h_{-1} and h_{+1}, such that $h_{+1}=h_{-1}=h_1$, the object in the k-th plane can be approximated by

$$\hat{o}_k = [i_k - c(i_{k-1} + i_{k+1}) \otimes h_{+1}] \otimes h_0^{-1} \tag{23}$$

where c is an adjustable constant, between 0.45 and 0.5.

This technique has the advantage of being very rapid, because it requires only two two-dimensional convolutions per plane. However, the efficiency of this method is greatly limited by the approximation in which light contributions from planes other than the two nearest neighbors are not taken into account. Recent advances in computer hardware have made it possible to use more sophisticated algorithms applied to the 3D light distribution in its entirety, in a reasonable time range.

4.4 Constrained Iterative Algorithms

The goal of this algorithm family is to develop a solution through an iterative process under positive constrains, which, when convolved by the known blurring function, will provide the acquired image. This type of algorithm is derived from the classical imaging equation (Eq. 13), assuming that the noise n_m is negligible [23, 24]. The classical imaging equation is then reduced to

$$i_m = \sum_l h_{l-m} o_l = a_m \tag{24}$$

4.4.1 The Jansson Van-Cittert Algorithm

By subtracting a_m from both sides of the equation, raising both sides to the power of p and by adding o_m to both sides, we get

$$o_m = o_m + (i_m - \sum_l h_{l-m} o_l)^p \tag{25}$$

Putting this equation into its iterative form results in

$$\hat{o}_m^{k+1} = K[\hat{o}_m^k + w_m(i_m - \sum_l h_{l-m} \hat{o}_l^k)^p] \tag{26}$$

where K is a normalizing energy constant and w_m a weighting function. w_m and p can be adjusted to enforce the non-negativity of the solution for all iterations.

If w_m=1–(i_k–A)2/A2, with A equal to the maximum value of i/2, and p=1, then this equation corresponds to the Jansson Van-Citter formula. In this case, the non-negativity constraint is forced by setting $\hat{o}_m^{k+1} = 0$ if $\hat{o}_m^{k+1} < 0$. The initialization of $\hat{o}_m^{k+1}$ is given by $\hat{o}_m^0 = i_m$. This iterative algorithm calculates a new estimate of the object as a function of the previous estimate, the acquired image and the known PSF, using an additive correction factor.

4.4.2 The Gold Algorithm

Based on exactly the same principle, the multiplicative formulation of constrained iterative algorithms can be obtained first by dividing both sides of the classical noise-free imaging equation (Eq. 24) by a_m and by raising both sides to the power of p, then by multiplying both sides by o_m, and finally by rewriting the result in its iterative form:

$$\hat{o}_m^{k+1} = K\hat{o}_m^k \frac{i_m}{\sum_l h_{l-m}\hat{o}_l^k}^p \tag{27}$$

For p=1, this equation corresponds to the Gold formula. Non-negativity condition is always ensured for optical objects ($\hat{o}^0$ positive), and, as for the additive case, the initialization of $\hat{o}_m^{k+1}$ is given by $\hat{o}_m^0 = i_m$.

First, both additive and multiplicative formulations of the iterative constraint algorithms suffer from slow convergence of the solution (although the multiplicative formulation gives a more rapid convergence). Second, they give poor results if the original data are noisy, particularly because noise not taken into account may create resonance and generate constructive artifactual signals. These two problems can be partially solved by adding a step to control noise throughout the iterative process. Practically, the first guess is filtered with a Gaussian or Wiener filter and each of four to seven iterations, depending on the signal-to-noise ratio, is smoothed using a Gaussian filter of variable width. The wider the filtering, the better the noise control is likely to be, but the less sharp the result. The user must take the decision concerning the acceptability of such a compromise, depending on the subsequent analyses to be performed.

4.5 Statistical Algorithms

Statistical information about the noise present in the images is incorporated into this family of algorithms. Like constrained iterative algorithms, they are recursive but they are built to determine an acquired object, blurred by the optical system and corrupted by random noise. The quantum nature of light results in the distortion of the image by noise. Noise is caused by photon counting (Poisson), detector readout (Gaussian) and analog-to-digital conversion (uniform). Statistical algorithms are based on finding an estimate $\hat{o}$ of the object o according to the nature of the noise. They can be classified into two subfamilies, according to the use or non-use of a regularization function. Both subfamilies are derived from the maximum likelihood estimation (MLE) algorithm, written to minimize the Poisson noise in the image. In the case of algorithms using a regularization function, noise is sometimes assumed to follow a Gaussian distribution for reasons of mathematical simplification [26]. The origins of these algorithms are described by the Bayesian theory of the

signal [27], in which the object o is statistically represented by its prior density function $P(o)$ and introducing the conditional density function $P(i|o)$ to model the blurred object i given the object o. Bayesian rules give the posterior density $P(o|i)$ of object o for a given blurred object i as

$$P(o|i) = \frac{P(i|o)\,P(o)}{P(i)} \tag{28}$$

This method is based on maximizing the probability function and estimating the maximum value of the object o, a posteriori, given the known image i. As $P(i)$ is independent of o, this is equivalent to minimizing the negative logarithm of the numerator of $P(o|i)$, providing a function Φ of the form

$$\Phi(o) = -\ln P(i|o) - \gamma \ln P(o) = L(i, o) + \gamma\Omega(o) \tag{29}$$

$L(i,o)$ is the likelihood estimation function of the object, $\Omega(o)$ is a smoothing function and γ is a regularization parameter. The likelihood function depends on the noise model: Poisson or Gaussian. It measures how well the estimate fits the acquired data. The smoothing function, also called the penalty function, attenuates the artifacts generated by noise amplification. γ is a balance between the need to fit the data and the need to stabilize the estimate. Setting Ω to 0 yields the maximum likelihood algorithm.

4.5.1 Maximum Likelihood Estimation Algorithms

Maximum likelihood estimation is a mathematical strategy for computing an object corrupted by noise. In the case of microscopy, the noise is linked to the statistical nature of quantum photon emission and follows a Poisson distribution, described by the following equation:

$$P_{Pois}(x|\mu) = \frac{\mu^x e^{-\mu}}{x!} \tag{30}$$

This equation gives the probability of obtaining a noisy datum x, given its noise-free averaged value μ. As each pixel constituting an acquired image is statistically independent from the others, it follows a Poisson distribution, and the whole image probability is then equal to the product of individual probabilities, giving

$$P_{Pois}(i|o) = P_{Pois}(i|a) = \prod_m P_{Pois}(i_m|a_m) = \prod_m \frac{a_m^{i_m} e^{-a_m}}{i_m!} \tag{31}$$

The log-likelihood function of the noise is obtained by taking the logarithm of the image probability:

$$L_{Pois}(i, o) = -\ln P_{Pois}(i|o) = \sum_m (a_m - i_m \ln(a_m) + \ln(i_m!)) \tag{32}$$

In the case of a Poisson noise process, the smoothing function Ω is set to zero and Φ is minimized by minimizing the likelihood function. The solution is straightforward and is computed by setting the derivative of the likelihood to zero, with respect to o_m, for fixed i, resulting in

$$\frac{\partial L(i,o)}{\partial o_m} = \sum_l \left(h_{m-l} \frac{i_l}{a_l} \right) - 1 = 0 \tag{33}$$

By adding 1 to both sides of the equation, raising both sides to the power p, adding o_m to both sides and writing the result in the iterative form, we obtain

$$\hat{o}_m^{k+1} = K \hat{o}_m^k \sum_l \left(h_{m-l} \frac{i_l}{\sum_n h_{l-n} \hat{o}_n^k} \right)^p \tag{34}$$

where $\hat{o}_m^0 = i_m$ and K is a constant ensuring energy conservation. The MLE ensures the non-negativity of the solution for optical objects ($\hat{o}^0$ positive), and no additional constraints are required. The Richardson and Lucy algorithm is obtained by assuming p=1.

These algorithms are the most frequently used to restore noisy data, mainly because they are easy and straightforward to use but also because the constraints they impose on noise statistics make them robust to noise. Nevertheless, they display very slow convergence (between 50 and 1000 iterations) and require more computing time per iteration than classical constrained iterative algorithms (two convolutions per iteration). Although, the use of a value greater than 1 for p makes the convergence faster, it also results in less stable convergence. With the absence of a regularization function Ω, the noise present during acquisition can lead to artifacts. In this case, the first estimate strongly influences the result and the first estimate should be smoothed with a Gaussian or Wiener filter, as for the iterative constrains algorithms, to prevent noise amplification during iteration. Another way of preventing such problems is to terminate the algorithm before convergence.

In the case of microscopy, Poisson noise is signal-dependent. It is therefore important to take into account the additive background b, mainly produced by the dark-field current of the detector, giving

$$\hat{o}_m^{k+1} = K \hat{o}_m^k \sum_l \left(h_{m-l} \frac{i_l}{\sum_n h_{l-n} \hat{o}_n^k + b_l} \right)^p \tag{35}$$

where b is the additive background image, which can be measured by taking dark images.

4.5.2 Algorithms Using a Regularization Function

One way to avoid convergence problems and to increase the speed of MLE algorithms is to add a regularization function. The goal is to minimize Eq. (29) in order to find a stable estimation of $\hat{o}$, and various strategies have been developed to achieve this. The noise is assumed to follow a Gaussian distribution rather than a Poisson distribution, to ensure that the algorithm can be solved mathematically and is compatible with Bayesian theory. This approximation has been validated for data with a high signal-to-noise ratio, and should in theory be restricted to such data. However, in practice, this family of algorithms work pretty well on noisy data, even though they are not optimized for such data. The corresponding Gaussian distribution of standard deviation σ is described by the following equation:

$$P_{Gaus}(x|\mu) = e^{-\frac{(i-\mu)^2}{2\sigma^2}} \tag{36}$$

Using an analog method for Poisson noise, the Gaussian log-likelihood function of the noise is given by

$$L_{Gaus}(i,o) = -\ln P_{Gaus}(i|o) = \frac{1}{2\sigma^2}\sum_m (i_m - a_m)^2 = \frac{1}{2\sigma^2}\|i - h \otimes o\|^2 \tag{37}$$

As for Poisson noise, the penalty function could be omitted and a Gaussian MLE algorithm could be written by simply minimizing the Gaussian likelihood. However, this is not really useful in practice because the MLE algorithm is better adapted. For a Gaussian noise distribution, the regularization function used may be the Gaussian density function $P(o)$, giving the quadratic penalty function

$$P(o) = \Omega(o) = \|o\|^2 \tag{38}$$

The Φ function to be minimized then becomes a quadratic function:

$$\Phi(\hat{o}) = \frac{1}{2\sigma^2}\|i - h \otimes \hat{o}\|^2 + \gamma\|\hat{o}\|^2 \tag{39}$$

equivalent to that obtained with matrix notation (Eq. 19). Its direct minimization yields the well known Wiener filter or unconstrained Tikhonov-Miller solution developed above, which has been shown to have practical limitations. Equation (19) can be minimized iteratively, adding the physical non-negativity constraint to the solution $\hat{o}_m^i \geq 0$.

The conjugate gradient method has been adapted for iterative minimization of the quadratic function Φ [28–30]. It is one of the most efficient iterative methods for identifying the extremes of a function of n variables, assuming that the gradient of the function can be calculated. This non-stationary method

moves forward by generating vector sequences of iterates (i.e., successive approximations to the solution), residuals corresponding to the iterates, and search directions used in updating the iterates and residuals. The iterates $\hat{o}^k$ are updated in each iteration by a multiple α^k of the search direction vector $\mathbf{p}^k$

$$\hat{\mathbf{o}}^k = \hat{\mathbf{o}}^{k-1} + \alpha^k \mathbf{p}^k \tag{40}$$

Correspondingly, the residuals $\mathbf{r}^k = \mathbf{b} - \mathbf{A}\hat{\mathbf{o}}^k$ are updated as

$$\mathbf{r}^k = \mathbf{r}^{k-1} - \alpha^k \mathbf{A}\mathbf{p}^k \tag{41}$$

with, in our case, $\mathbf{A} = (\mathbf{H}^T\mathbf{H} + \eta)$ and $\mathbf{b} = \mathbf{H}^T\mathbf{i}$.

In the absence of nonlinear constraints, an optimal value of α^k can be calculated analytically and is given by

$$\alpha^k = -\frac{\mathbf{p}^{k^T}\mathbf{r}^{k-1}}{\mathbf{p}^{k^T}\mathbf{A}\mathbf{p}^k} \tag{42}$$

However, if there is a nonlinear non-negativity constraint on the estimate, this value is no longer valid, resulting in very slow convergence of the solution [26], rendering this algorithm much less useful than the standard MLE algorithm.

The iterative constrained Tikhonov Miller (ICTM) algorithm has been used to take into account the non-negativity constraint of $\hat{\mathbf{o}}$ and to generate a better estimate of α^k [28, 30]. It involves a one-dimensional iterative minimization algorithm, like the Brent or Gold algorithm [32], and aims to minimize $\Phi(C(\hat{\mathbf{o}}^{k-1} + \alpha^k \mathbf{p}^k))$, with $C(.)$ the non-negativity constraint operator, which sets the negative values of its argument to zero. The final algorithm consists of a main iterative loop for calculating the conjugate direction, and a subiterative loop that finds the best estimate of α^k and calculates the new estimate of $\hat{\mathbf{o}}$. This increases the computation time because, for each estimate of α^k in the subiteration loop, a complete evaluation of $\Phi(C(\hat{\mathbf{o}}^{k-1} + \alpha^k \mathbf{p}^k))$ must be carried out, and this is the most cumbersome part of the algorithm. Moreover, this algorithm lacks mathematical rigor because the gradient of $\Phi(\hat{\mathbf{o}}^k)$ is used to minimize the gradient of $\Phi(C(\hat{\mathbf{o}}^k))$.

An alternative approach to increasing computation speed by increasing the speed of determination of α^k was investigated by Veerver et al. [26]. This method involves determining the value of α^k that sets the gradient to zero in the search direction, and then solving

$$\mathbf{p}^{k^T} \nabla \Phi (C(\mathbf{o}^{k-1} + \alpha^k \mathbf{p}^k)) = 0 \tag{43}$$

which gives

$$\alpha^k = -\frac{\mathbf{p}^{k^T}\mathbf{T}(\mathbf{o})\mathbf{r}^{k-1}}{\mathbf{p}^{k^T}\mathbf{T}(\mathbf{o})\mathbf{A}\mathbf{T}(\mathbf{o})\mathbf{p}^k} \tag{44}$$

where $\mathbf{T}(\mathbf{o})$ is a diagonal matrix defined by

$$\mathbf{T}(\mathbf{o})_{ij} = \begin{cases} 1 & \text{if i = j and } \mathbf{o}_i > 0 \\ 0 & \text{otherwise} \end{cases} \tag{45}$$

This direct solution is more rigorous mathematically than that for ICTM algorithms. It is also much faster because no subiteration loop is required.

In contrast to the situation for Poisson noise, the variance of Gaussian noise is, by definition, independent from the signal. Therefore, the background image can be omitted in each of the equations without changing the noise properties, simply by subtracting it from the data in the preprocessing step.

4.6 Blind Deconvolution Algorithms

In the blind deconvolution approach, the object and the PSF are assumed to be unknown and are estimated throughout the iterative process [34–36]. The algorithm uses the standard MLE algorithm described above, together with a PSF estimation for each iteration. The object is computed, using the MLE estimation, as follows:

$$\hat{o}_m^{k+1} = K\hat{o}_m^k \sum_l \left(\hat{h}_{m-l}^k \frac{i_l}{\sum_n \hat{h}_{l-n}^k \hat{o}_n^k} \right) \tag{46}$$

Using exactly the same mathematical reasoning, PSF is estimated by maximizing the log likelihood function with respect to h_m, which gives

$$\hat{h}_m^{k+1} = \frac{\hat{h}_m^k}{N} \sum_l \left(\hat{o}_{m-l}^k \frac{i_l}{\sum_n \hat{o}_{l-n}^k \hat{h}_n^k} \right) \tag{47}$$

where N is a normalization constant relating to the unit volume. Object initialization is performed using $\hat{o}_m^0 = i_m$, and the first estimate of PSF $\hat{h}_m^0$ is calculated theoretically from the microscope parameters. Like the standard MLE algorithm, the non-negativity of both $\hat{o}_m^{k+1}$ and $\hat{h}_m^{k+1}$ are ensured. Additive constraints on the PSF can be imposed, such as both axial circular symmetry and frequency band-limited properties, which can be used to check the PSF. These constraints are added at each iteration, after the computation of the new estimate $\hat{h}_m^{k+1}$. Axial circular symmetry is achieved plan-by-plan, by averaging the values equidistant from the middle of the image, where the optical axis should exist. The frequency band-limited constraint is imposed by setting all the values of the Fourier transformation of $\hat{h}_m^{k+1}$ such that they lie above the known frequency cutoff. In three-dimensional microscopy, lateral and axial resolutions are different, and the PSF can be filtered separately in each of the two directions.

Like the standard MLE algorithm, this family of algorithms suffers from slow convergence and the estimates obtained are not stable. First guess smoothing and regularization functions can be applied to increase the convergence speed, as described above.

This family of algorithms may be used for non-specialist purposes, or when the point spread function is unknown. It takes twice as long as the MLE per iteration but can produce better results than the use of a theoretical PSF, especially if unpredicted aberrations are present. Nevertheless, we always recommend that the acquisition system be characterized and calibrated (see above on PSF determination), to minimize aberrations before acquisition, because the better the acquisition, the better the result of the deconvolution is likely to be, regardless of the algorithm used.

4.7 Results

In this section, we have tested various algorithms, using commercial packages. It is very difficult to compare algorithms because the results obtained depend heavily on image quality (signal-to-noise ratio, sampling), and on algorithm parameters and optimizations. Which criteria should be used to compare images? Image quality, which is very difficult to assess for biological objects, is not the only parameter in practice. Speed is also of great importance because in some cases it is preferable to use a given algorithm simply because it is ten times faster than another "more rigorous" algorithm. It is also difficult to compare the speeds of the different algorithms, because this speed depends on the way the algorithms are implemented, optimizations and stopping criteria, and a given algorithm may give different results and execution speeds when implemented via different software packages. We will therefore avoid detailing speeds here. We will instead show results obtained with different families of algorithms, and will try to assess the advantages and limitations of each, and their robustness to noise. However, we will also present some typical artifacts that may arise.

Figure 15 displays deconvolution results obtained with five algorithms, from the various families described above. We display three optical sections and one axial cross section for each. We have also measured intensity profiles and added arrows to illustrate in more detail the efficiency of these algorithms and to draw attention to specific parts of the images.

Artifacts may arise for various reasons. For example, the algorithm chosen may not be efficient enough to process the data in the presence of too much noise. Alternatively, the choice of algorithm parameters may be poor, PSF estimation may be inaccurate or the data may have been subsampled. There is little point in trying to illustrate all these artifacts on real samples because their appearance depends on object morphology and noise level. We have discussed fully the key role played by noise and incorrect PSF estimation in the generation of artifacts. To illustrate these points, Fig. 16 shows the result of deconvolution on images of fluorescent microbeads internalized by a cell before fixa-

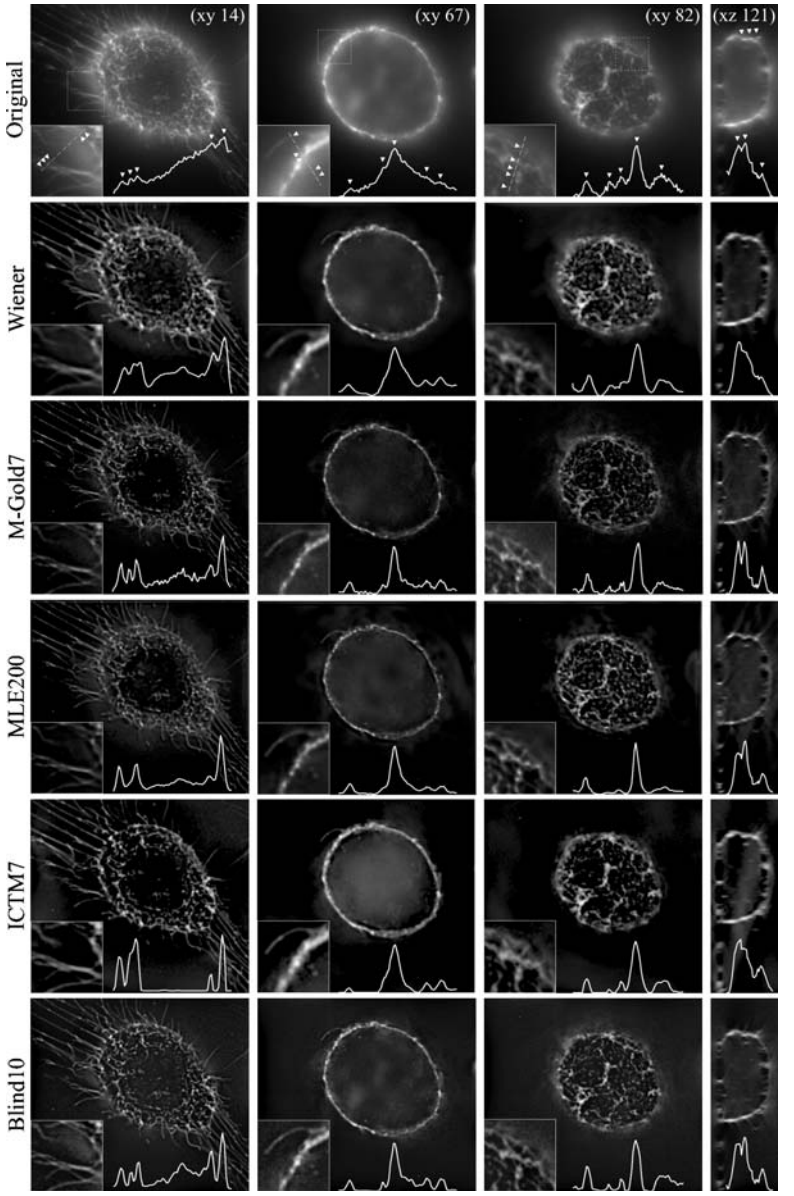

Fig. 15 Image deconvolution of a fixed MDCK cell labeled with concanavalin A – FITC. Images were acquired with a 3D microscope, as described in the text. From *left to right*: optical sections of the bottom (on the coverslip), middle and top of the cell, and axial cross-section of the same cell. From *top to bottom*: Original data, and data restored using: the Wiener invert filter, the modified Gold iterative constrained algorithm with 7 iterations (Metamorph, Universal Imaging), the MLE algorithm with 200 iterations, the quick ICTM algorithm with 7 iterations (Huygens, SVI) and finally the blind MLE deconvolution algorithm with 10 iterations (Autodeblur, Autoquant)

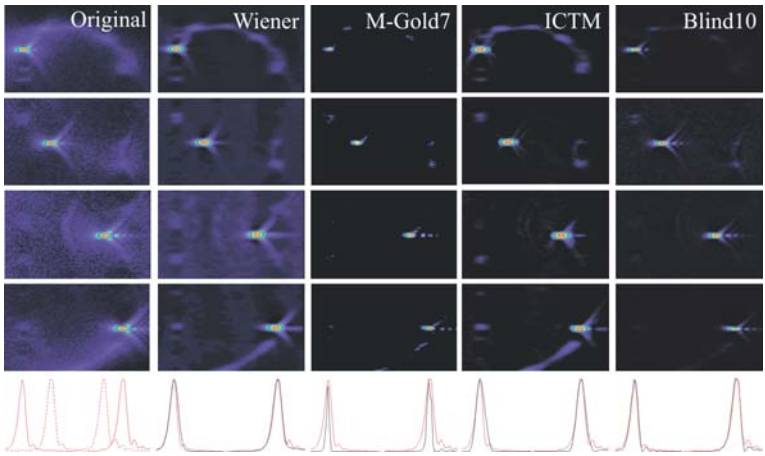

Fig. 16 Image deconvolution of fluorescent microbeads located at various distances from the coverslip. Rhodamine microbeads, 100 nm in diameter, were internalized within an MDCK cell before fixation. From *left to right*, axial cross-sections on original data, and data restored using: the Wiener invert filter, the modified Gold iterative constrained algorithm with 7 iterations (Metamorph, Universal Imaging), the quick ICTM statistical algorithm with 7 iterations (Huygens, SVI) and finally the blind MLE deconvolution algorithm with 10 iterations (Autodeblur, Autoquant). For all the algorithms, except for the blind approach, the PSF was modeled using a microbead located on the coverslip. The *bottom line* displays intensity profiles measured along bead cross-sections

tion and located at various distances from the coverslip. This indicates the efficiency of the deconvolution algorithms in terms of axial resolution, and illustrates the artifacts that arise when a single PSF model is used, given that axial shift invariance is assumed in all the algorithms. As expected, efficiencies decreased and artifacts increased with increasing distance of the bead from the coverslip (Fig. 16).

Finally, to illustrate robustness of the algorithms to noise, deconvolution results obtained with four different algorithms applied to image stacks acquired with different exposure times are shown in Figs. 17 and 18. As expected, the signal-to-noise ratio of the images considerably affects the quality of the results for most of the algorithms. Moreover, some typical artifacts become visible on images with low signal-to-noise ratios, with the emergence of a background texture with an amplitude in the order of magnitude of the signal. As predicted by theory, statistical algorithms, which require heavier computation, are more robust to noise. Nevertheless, the addition of a noise control parameter to constrained iterative algorithms increases their robustness to noise, and good results can be obtained in a very short time.

It is not easy to compare algorithms. However, although it is impossible to draw definitive conclusions concerning the efficiencies of algorithms from only a few data sets, a few general comments can be made. First, for all the algo-

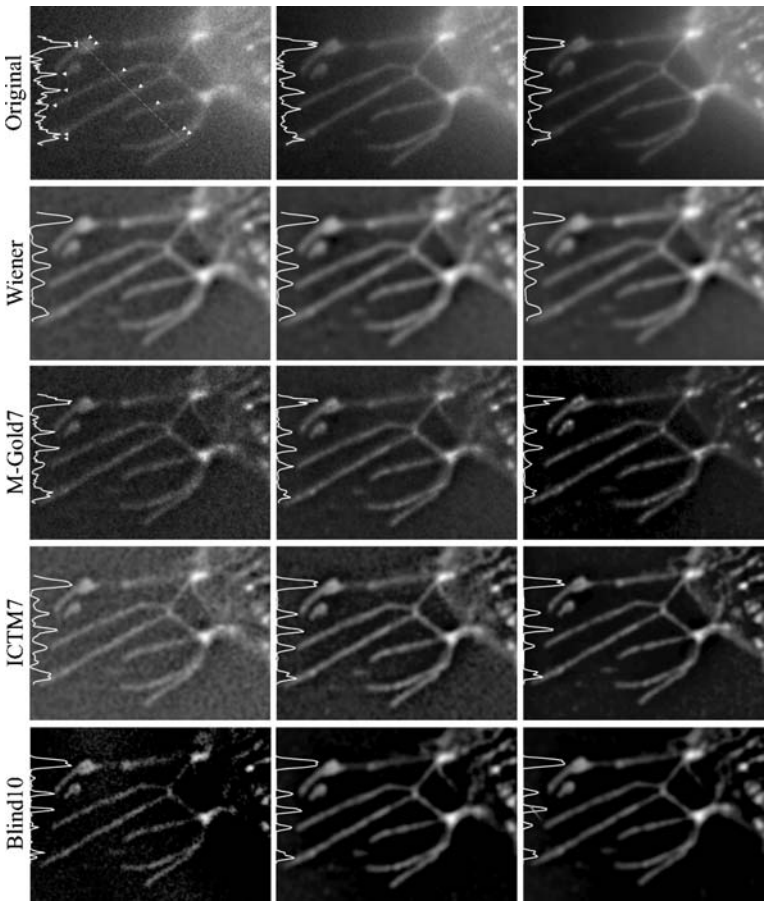

Fig. 17 Deconvolution of image stacks acquired with different exposure times, using four different algorithms. Original images of a single plane acquired for, from *left to right*, 50 ms, 100 ms and 200 ms per plane. From *top to bottom*, images restored using: the Wiener invert filter, the modified Gold iterative constrained algorithm with 7 iterations (Metamorph, Universal Imaging), the ICTM algorithm with 7 iterations (Huygens, SVI) and finally the blind MLE deconvolution algorithm with 20 iterations (Autodeblur, Autoquant)

rithms and processed images presented, deconvolution clearly improved image quality. It enhanced contrast and decreased blurring, mainly in the axial direction. Such an improvement should always occur, provided that the PSF estimate used is correct. Even planes distant from the coverslip, for which we know the PSF is not perfectly valid, do not present strong artifacts. Second, the Wiener invert filter is clearly much less efficient than other iterative methods. However, the ability of this algorithm to reduce noise nonetheless renders it useful for first guesses for iterative algorithms. All noisy data were improved, even with classical iterative algorithms such as MGold, which includes a noise control

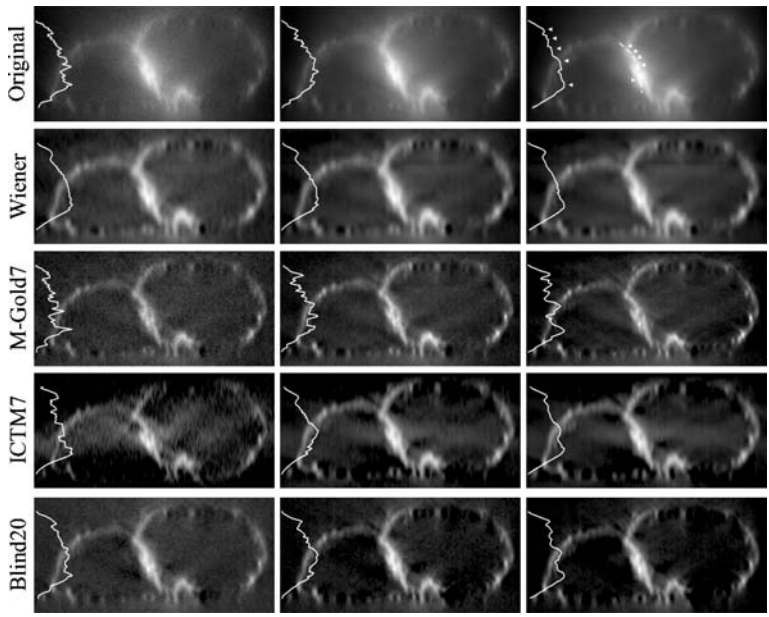

Fig. 18 Deconvolution of image stacks acquired with different exposure times, using four different algorithms. Axial Cross sections of original image stacks acquired for, from *left to right*, 50 ms, 100 ms and 200 ms per plane. From *top to bottom*, cross sections of restored stacks using: the Wiener invert filter, the modified Gold iterative constrained algorithm with 7 iterations (Metamorph, Universal Imaging), the ICTM algorithm with 7 iterations (Huygens, SVI) and finally the blind MLE deconvolution algorithm with 20 iterations (Autodeblur, Autoquant)

parameter. Moreover, as if slightly less robust to noise than statistical algorithms, MGold greatly improves the image quality in the axial direction. MLE algorithms give good results, but are not very useful in the absence of a regularization parameter, due to very slow convergence. Even after 200 iterations the MLE gave unsatisfactory results, whereas only seven iterations of the QICTM gave better results. All the results obtained with the blind deconvolution algorithm were good, although some artifacts began to appear with noisy data. Nevertheless, microscope characterization must still be carried out correctly as this step is crucial for collecting "perfect" data and hence obtaining good final results. Finally, even when the estimate of PSF used is accurate and acquisition conditions are perfect, artifacts may arise in the restored data. As a general rule, all the structures present in the restored data should be visible in the original data, even if they are unclear. Thus, if a new structure appears, it is certainly an artifact.

4.8 Deconvolution of Large Data Sets by Distributed Computing

The deconvolution technique has become so common that it has now essentially been integrated into microscopy and has become a part of the acquisition process itself. This so-called "deconvolution microscopy" is based on recent increases in the computational power available. In parallel, fluorescence microscopy has made a major leap forward in terms of multidimensional data collection, greatly increasing the amount of data to be processed. It is now not unusual to obtain gigabytes of data in thousands of files in the space of an hour, and the difficulty lies less in processing several "huge" stacks than in processing the growing flux of stacks generated by this ultra-fast microscopy. Living-cell time-lapse microscopy is now faced with the same problems as nuclear physics studies involving huge particle accelerators: how to almost instantaneously capture and process huge amounts of collected data. Of course, the order of magnitude of the problem differs between instruments: whereas light microscopy deals with terabytes (10^6 megabytes) of data, particle accelerators deal with petabytes (10^9 megabytes). However, in the near future, most cell biology research laboratories will be equipped with a wide variety of rapid microscopes, whereas only a few particle accelerators are available worldwide, so the challenge is probably equally great in both disciplines.

The deconvolution of such large amounts of data is critical and may become a brake on progress. The computer responsible for image processing is generally connected to a local area network (LAN). Frequently, other workstations in this LAN are not in full-time use: at night, in particular, most computers are idle. This "down time" could be used more effectively. Moreover, with the developments of low-cost PC farms, it is becoming easier and cheaper to obtain high computational capacities. We have developed a method for distributed computations to take advantage of these possibilities [37].

In our approach, we do not parallelize the deconvolution algorithm itself to increase the deconvolution speed of each stack. Instead, we distribute independent tasks, at the image stack level. Thus, our parallel calculations are "coarse-grained", the computational element being a single stack. Basically, processing jobs are queued into a pipeline. At its endpoint, job consumer threads (A-N) concurrently invoke the deconvolution of queued stacks on remote servers (remote computers A-N) (Fig. 19).

Our computational model is derived from some early attempts to distribute, over a network of computers, numerical calculations requiring the transfer of non-negligible amounts of data between client and servers [38, 39]. However, recent advances in network technologies have increased reliability and performances. In particular, web-based approaches to distributed computing are even beginning to emerge [40].

However, network performance still presents an obstacle because each stack must be sent from the client application to a server before remote processing; transport time is therefore non-negligible. The extent to which speed is in-

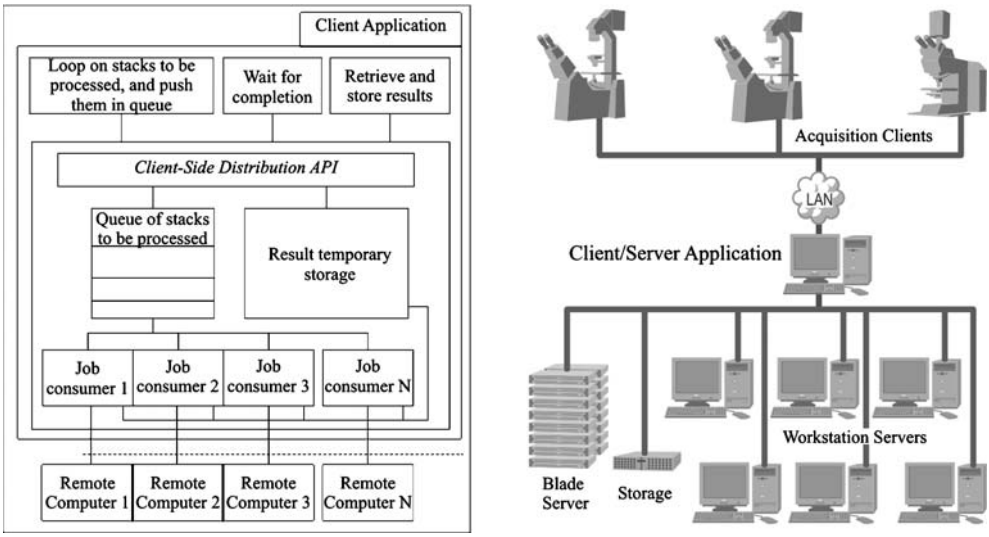

Fig. 19 Computational model of the distribution process (*left*) and distributed deconvolution microscopy architecture (*right*)

creased clearly depends on the time T_P to process a single stack and the time T_N to send this stack back and forth between the client and a server. Figure 20 shows a simulation of the "speedup factor" as a function of the ratio T_N/T_P.

The major issue when assessing the potential value of distributed computation is this T_N/T_P ratio. To visualize this mentally, just consider T_P as the "parallelizable" part of the computation, whereas T_N is "uncompressible" because however many computers there are, there is only one physical network link available. When T_N/T_P is low, this means that the algorithm is complex with respect to the amount of data to be transferred and that the process may be accelerated effectively by using multiple computers. When T_N/T_P is high, the problem is less a matter of algorithmic complexity than of data transfer performance; in such cases, shared memory or massively parallel computers may be more appropriate.

Although it is sometimes argued that network technology (and speed) will improve in the future, it should be noted that processors are likely to undergo similar improvements. Thus, if T_N/T_P is low for a given computational problem in 2004, it will probably not be significantly better for the same problem in 2014 – just imagine the "race towards performance" in which both processor and network manufacturers are engaged… The outcome clearly depends on the "winner of the race".

To illustrate the method, we processed 120 stacks of 1.4 Mb each (160 Mb of raw data) off-line using the modified Gold algorithm with 10 iterations and the MLE algorithm with 50 iterations. One to eight similar remote computers (PIV-2 GHz) linked on a 1 Gb/s LAN were used to assess the increase in speed.

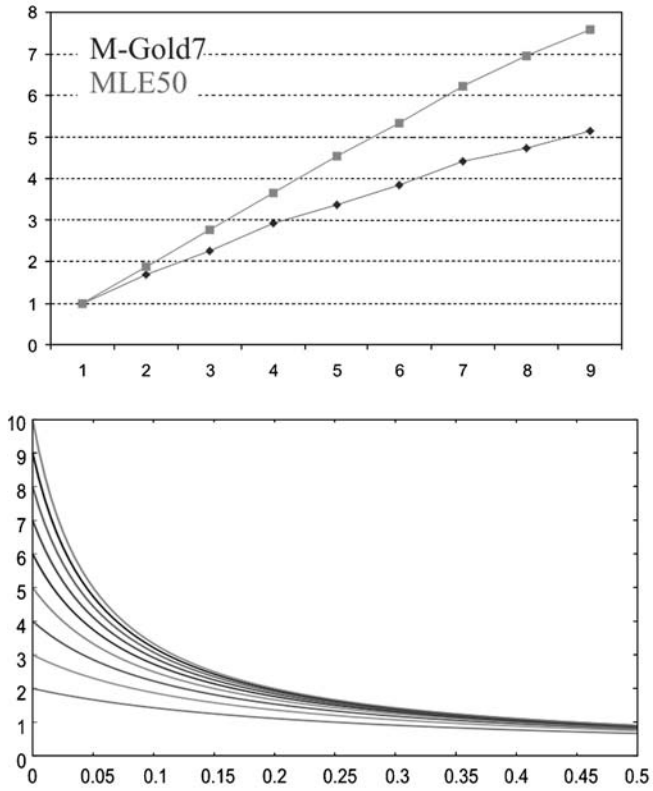

Fig. 20 *Top*: Measured speedup factor using one to eight remote similar computers in parallel, for 2 different algorithms: MGold with 7 iterations and MLE with 50 iterations. Computation was achieved using 120 stacks of 1.4 Mb each, and computers connected via a 1 Gb/s LAN. *Bottom*: Simulation of the speedup factor as a function of the ratio T_N/T_P for two to ten remote servers

A stack of 500×400 pixels × 9 planes was acquired every second over a 2-min period with only 50 ms exposure time per plane. The acquisition of each stack in z-streaming mode took less than 500 ms, allowing more than 500 ms for fluorescence relaxation. Figure 20 shows the measured speedup factor as a function of the number of remote servers. The speedup factor is defined as the time required to restore all the stacks in sequential mode, divided by the time measured to restore all the stacks in parallel mode. The only difference between the algorithms is the computing time per stack.

In the fastest case, it took only 1 min 45 s to process all the data using eight remote servers plus the client computer, rather than about 9 min in sequential mode, giving a speedup factor greater than 5.

In conclusion, for this typical high-speed time-lapse microscopy experiment, the total acquisition time was greater than the total processing time. This technology could therefore be seen as leading the way towards online process-

ing. We imagine that in the very near future, it will be possible to visualize the deconvolution during the acquisition. Achieving on-screen real-time navigation within the 3D model of a live cell, the dream may finally become a reality.

Acknowledgments Vincent Fraisier, Fabrice Cordelières, Henri Magnin, Jean Salamero, Zvi Kam, Nate O'Connor, Jeff Stuckey, Tim Holmes, David Biggs, Jan De Mey, Pascal and Joy Jaillon.

References

1. Agard DA (1984) Ann Rev Biophys Bioeng 13:191
2. Chalfie M (1994) Science 263:802
3. Cubitt AB (1995) Trends Biochem Sci 20:448
4. Ormo M (1996) Science 273:1392
5. Pawley JB (1995) Handbook of biological confocal microscopy. Plenum, New York
6. Wilson T (1990) Confocal microscopy. Academic Press, London
7. Kino GS (1995) Intermediate optics in Nipkoff disk microscopes In: Pawley JB (1995) Handbook of biological confocal microscopy. Plenum, New York, p 155
8. Wallace W, Schaefer LH, Swedlow JR (2001) BioTechniques 31:1075
9. McNally JG, Karpova T, Cooper J, Conchello JA (1999) Methods 19:373
10. Sheppard C, Gan X, Gu M, Roy M (1995) In: Pawley JB (1995) Handbook of biological confocal microscopy. Plenum, New York, p 363
11. Born M, Wolf E (1964) Principle of optics. Pergamon, New York
12. Inoué S, Spring KR (1997) Video-microscopy. Plenum Press, New York
13. Erhardt A, Zinser D, Komitowski D, Bille J (1995) Appl Opt 24:194
14. Hiraoka Y, Sedat JW, Agard D (1990) Biophys J 57:325
15. Gibson SF, Lanni F (1991) J Op Soc Am 8:1601
16. Scalettar BA, Swedlow JR, Sedat J, Agard DA (1996) J Microsc 182:50
17. Kam Z, Hanser B, Gustafsson MGL, Agard DA, Sedat J (2001) Proc Natl Acad Sci USA 98:3790
18. Hanser B, Gustafsson M, Agard D, Sedat J (2003) Opt Lett 28:801
19. Visser TD, Groen FCA, Brakenhoff GJ (1991) J Microsc 163:189
20. Carrington W (1990) Proceedings of SPIE The International Society for Optical Engineering 1205:72
21. Gonzalez R, Woods R. (1993) Digital image processing. Addison Wesley
22. Castelman KR (1979) Digital image processing. Prentice Hall, Englewood Cliffs
23. Agard DA, Hiraoka Y, Shaw P, Sedat JW (1989) Methods Cell Biol 30:353
24. Jannson PA, Hunt RM, Plyler EK (1970) J Opt Soc Am 60:596
25. Meinel ES (1986) J Opt Soc Am A. 3:787
26. Verveer P, Jovin T (1997) J Microsc 188:191
27. Richardson W (1972) J Opt Soc Am 62:55
28. Lagendikk RL (1990) PhD Thesis
29. Carrington WA, Lynch RM, Moore EDW, Isenberg G, Fogarty KE, Fay ES (1995) Science 268:1483
30. Van der Vort H, Strasters K (1995) J Microsc 178:165
31. Verveer P, Gemkow M, Jovin T (1999) J Microsc 193:50
32. Press WH, Flannery BP, Teukosky SA, Vetterling WT (1999) Numerical recipes in C. University Press, Cambridge UK

33. Verveer P, Gemkow M, Jovin T (1999) J Microsc 193:50
34. Holmes TJ (1992) J Op Soc Am A 9:1052
35. Krishnamurthi V, Liu YH, Bhattacharyya S, Turner JN, Holmes TJ (1995) Appl Opt 34:6633
36. Holmes TJ, Bhattacharyya S, Cooper JA, Hanzel D, Krishnamurthi V, Lin WC, Roysam B, Szarowski DH, Turner JN (1995) In: Handbook of biological confocal microscopy. Plenum, New York, p 389
37. Sibarita JB, Magnin H, De Mey J (2002) IEEE Proc
38. Magnin H (1991) PhD Thesis INPG, University of Grenoble, France
39. Magnin H, Coulomb JL (1990) Proc. STRUCOME conference, Paris, France, p 563
40. Natrajan A, Crowley M, Wilkins-Diehr N, Humphrey MA, Fox AD, Grimshaw AS, Brooks CL (2001) Proc 10th IEEE International Symposium on High Performance Distributed Computing, San Francisco